

¹ **MicroBooNE: Neutron Induced Cosmogenic π^0 's**

² **Ryan A.Grosso**

³ Submitted in partial fulfillment of the
⁴ requirements for the degree
⁵ of Doctor of Philosophy
⁶ in the Graduate School of Arts and Sciences

⁷ **UNIVERSITY OF CINCINNATI**

⁸ 2017

9

10

©2017

11

Ryan A.Grosso

12

All Rights Reserved

¹³ Table of Contents

¹⁴	List of Figures	iii
¹⁵	List of Tables	v
¹⁶	1 Introduction	1
¹⁷	2 Neutrinos & Neutrino Oscillations	3
¹⁸	2.1 The History the Neutrino	3
¹⁹	2.2 Discovery of the Neutrino	5
²⁰	2.3 Neutrinos in the Standard Model	8
²¹	2.4 Neutrino Interactions	9
²²	2.5 Neutrino Mass and Flavor Oscillations	12
²³	2.6 Sterile Neutrinos	17
²⁴	3 The MicroBooNE Detector	18
²⁵	3.1 Brief History of LAR-TPC's	18
²⁶	3.2 Introduction	19
²⁷	3.3 Time Projection Chamber	20
²⁸	3.4 Light Collection	26
²⁹	3.5 Electronics Readout	28
³⁰	4 Booster Neutrino Beam	30
³¹	4.1 Primary Beam, Target and Horn	31
³²	4.2 Neutrino Flux Prediction	32

³³	5 Low Energy Excess and Relevant Cross Sections	35
³⁴	5.1 Overview	35
³⁵	5.2 LSND Excess	35
³⁶	5.3 Miniboone Excess	37
³⁷	5.4 Neutral Current π^0 production	38
³⁸	5.5 NC-Pi0 in Carbon vs Argon	40
³⁹	6 Cosmogenic π^0's at MicroBooNE	41
⁴⁰	6.1 Motivation	41
⁴¹	6.2 Monte Carlo Simulation	42
⁴²	6.3 Traditional Reconstruction	44
⁴³	6.4 Wire Cell Imaging	45
⁴⁴	6.5 Pattern Reconcition	46
⁴⁵	6.5.1 Shower Reconstruction	46
⁴⁶	6.5.2 Single π^0 Reconstruction	46
⁴⁷	7 Results	51
⁴⁸	7.1 Reconstructed Variables	51
⁴⁹	7.2 Performance	51
⁵⁰	8 Conclusions	52
⁵¹	8.1 Conclusion	52
⁵²	8.2 Outlook	52
⁵³	I Appendices	53

⁵⁴ List of Figures

55	2.1 Cowan and Reines first proposed neutrino experiment.	5
56	2.2 The Hadron production cross section around the Z^0 resonance from LEP.	7
57	2.3 The Standard Model	9
58	2.4 Charge and Neutral Current Interactions	12
59	2.5 This plot shows the appearance and disappearance curves for a 2-flavor ap-	
60	proximation as a function of baseline. The values of $\Delta m^2 = 0.0025\text{eV}^2$ and	
61	$\sin^2 \theta = 0.14$ are used.	14
62	2.6 Neutrino Mass Hierarchy	16
63	3.1 Diagram of a Time Projection Chamber	19
64	3.2 MicroBooNE TPC	21
65	3.3 MicroBooNE wires measured linear mass density	22
66	3.4 Tensioning system	23
67	3.5 Multiple wire planes installed in MicroBooNE	24
68	3.6 MicroBooNE tension measuring device	25
69	3.7 MicroBooNE tension map	26
70	3.8 MicroBooNE tension histogram	26
71	3.9 PMT optical unit	27
72	3.10 PMT optical unit	28
73	3.11 Detector Electronic layout	29
74	4.1 The Booster Neutrino Campus	30
75	4.2 BNB Target	32

76	4.3	Booster Neutrino Beamline	33
77	4.4	BNB Target	34
78	5.1	LSND Excess	36
79	5.2	MiniBooNE Event topology	38
80	5.3	MiniBooNE excess for ν and $\bar{\nu}$	39
81	5.4	pi0production	40
82	6.1	Icarus Cosmic π^0	43
83	6.2	Cosmic π^0 production by parent process	44
84	6.3	pi0Photon	47
85	6.4	Reconstructed energy sum and energy product for shower pairs	48
86	6.5	pi0Photon	49
87	6.6	pi0Photon	50

List of Tables

88	4.1 Beam Production Systematics	34
----	---	----

⁹⁰ Chapter 1

⁹¹ Introduction

⁹² This thesis describes work towards electromagentic shower reconstruction and steps towards
⁹³ a neutral current single π^0 cross section measurement motivated from reconstruction tech-
⁹⁴ niques used for neutron induced cosmogenic π^0 analysis. This thesis will use data from
⁹⁵ the MicroBooNE Liquid Argon Time Projection Chamber(LArTPC) located at the Fermi
⁹⁶ National Accelerator in Batavia, Il.

⁹⁷

⁹⁸ To begin, Chapter 2 will provide some background about the neutrino. We will begin by
⁹⁹ presenting the initial premise for the need of a neutrino-like particle. Then, we will describe
¹⁰⁰ the theoretical framework used to address how they interact the standard model. Finally we
¹⁰¹ will present the phenomenon known as neutrino oscillation and provide some mathematical
¹⁰² framework to describe it. Chapter 3 begins with a brief history of the LArTPC detector
¹⁰³ technology and it's use as a high precision neutrino detector. The chapter continues to
¹⁰⁴ explain in depth the various subsystems that constitute the MicroBooNE detector. Chapter
¹⁰⁵ 4 will describe how a neutrino beam is produced and delivered to the MircoBooNE detector.
¹⁰⁶ It will focus on Fermilab's Booster Neutrino Beam(BNB) which generates a beam of nearly
¹⁰⁷ pure ν_μ or $\bar{\nu}_\mu$ around 1GeV in average energy. Chapter 5 will present in detail the claims
¹⁰⁸ of the electromagnetic ν_e -like excess first seen by the LSND experiment and then later
¹⁰⁹ verified by the MiniBooNE experiment. This chapter will also discuss the neutral current
¹¹⁰ cross section, which is the main background in the MiniBooNE excess claim. Chapter
¹¹¹ 6 will introduce MicroBooNE's cosmogenic background and motivate the importance of

understanding the cosmic rate. Here, we will also discuss the motivation to use cosmic π^0 events as a means of calibrating the detector energy scale. The cosmic backgrounds are addressed for the oscillation analysis and a future neutral current 1 π^0 measurement. Next, this chapter will address simulation, reconstruction, and event selection. Chapter 7 will present results from MicroBooNE cosmics data addressing the cosmic π^0 rate from neutral induced events.

¹¹⁸ **Chapter 2**

¹¹⁹ **Neutrinos & Neutrino Oscillations**

¹²⁰ **2.1 The History the Neutrino**

¹²¹ The story of the neutrino began in Paris on a cloudy winter day in the year 1896. Parisian
¹²² native, Henri Becquerel was experimenting with uranium salts and investigating the newly
¹²³ discovered x-ray radiation. [] He hypothesized that when the salts were energized by sun-
¹²⁴ light they would produce the x-ray radiation. This hypothesis was disproven on the cloudy
¹²⁵ February 27th day when his experiment still detected radiation emitting from the salts in
¹²⁶ the absence of the sun. Becquerel had discovered radioactivity. In the coming years, this
¹²⁷ phenomena was supported by the work of Marie and Pierre Curie in studying the radioac-
¹²⁸ tivity of the element Thorium which lead to their discovery of the elements Polonium and
¹²⁹ Radium. These discoveries would later win Becquerel and the Currie's the 1903 Nobel Prize
¹³⁰ in Physics.

¹³¹

¹³² After radioactivity became an accepted phenomena in the science community, Ernst
¹³³ Rutherford discovered that radioactive decay products came in two different forms. He
¹³⁴ labeled them as α -decay and β -decay. At the time, beta decay was believed to be a two body
¹³⁵ decay where a nucleus A decays into a lighter nucleus A' and a β -particle(electron). The
¹³⁶ outgoing energy of the electron from a two body decay is given by equation 2.1. Assuming
¹³⁷ conservation of energy, the value of the outgoing energy should be a discrete.

$$E_e = \frac{m_A^2 + me^2 - m_{A'}^2}{2m_A} \quad (2.1)$$

138 In 1914, James Chadwick had discovered that the energy spectrum of the β -particles
 139 were continuations as opposed to mono-energetic. While some scientist were willing to
 140 abandon the requirement of energy conservation, others found this to be an unpalatable
 141 solution. Unable to attend the 1930 Tubingen physics conference in Germany, Wolfgang
 142 Pauli wrote a letter to the attendees in which he proposed the first idea of the neutrino.
 143 An excerpt from his famous December 4th letter is translated from German below [].

144 I have hit upon a desperate remedy to save the “exchange theorem” of statistics
 145 and the law of conservation of energy. Namely, the possibility that there could
 146 exist in the nuclei electrically neutral particles, that I wish to call neutrons,
 147 which have spin 1/2 and obey the exclusion principle and which further differ
 148 from light quanta in that they do not travel with the velocity of light. The
 149 mass of the neutrons should be of the same order of magnitude as the electron
 150 mass and in any event not larger than 0.01 proton masses. The continuous beta
 151 spectrum would then become understandable by the assumption that in beta
 152 decay a neutron is emitted in addition to the electron such that the sum of the
 153 energies of the neutron and the electron is constant...

154 In 1932, Chadwick discovered the neutron we know of today. Unfortunately, this neutron
 155 was too heavy to be the particle that Pauli had proposed. Expanding on Pauli’s work, Enrico
 156 Fermi proposed a more complete picture of beta decay and renamed Pauli’s ‘neutron’ to
 157 what is commonly called a *neutrino*. Fermi’s theory directly coupled the neutron with a
 158 final state proton, electron, and neutrino. This theory of beta decay, $n \rightarrow p + e^- + \bar{\nu}_e$
 159 preserves the law of conservation of energy and would later prove to be a more accurate
 160 descriptor of the process.

¹⁶¹ **2.2 Discovery of the Neutrino**

¹⁶² Measuring and detecting neutrinos is a tricky business. In the 1950's, Clyde Cowan and
¹⁶³ Frederick Reines set out to directly measure neutrino interactions for the first time. If a free
¹⁶⁴ neutrino existed, they hypothesized that they could detect the byproducts from the inverse
¹⁶⁵ beta decay $\bar{\nu}_e + p \rightarrow e^+ + n$. They realized that such a measurement would require a very
¹⁶⁶ intense neutrino source and a large detector. Their first proposal, which was approved, was
¹⁶⁷ to detonate a nuclear bomb to supply the large, instantaneous source of neutrinos. A large
¹⁶⁸ detector filled with liquid scintillator would free fall down a mind shaft recording flashes
¹⁶⁹ of light from the ionizing positrons before landing on a bed of feathers and foam rubber.
¹⁷⁰ The original experimental schematic is shown in Figure 2.1. At that time, the theorized
¹⁷¹ neutrino cross section was $10^{-43} \text{ cm}^2/\text{proton}$ while the existing measured limit was still 7
¹⁷² orders of magnitude short in sensitivity. The bomb experiment would have worked but
¹⁷³ could not provide the level of sensitivity required to confirm detection for neutrino cross
¹⁷⁴ sections below $10^{-39} \text{ cm}^2/\text{proton}$. This was due to background interactions that came in
¹⁷⁵ time directly from the bomb.

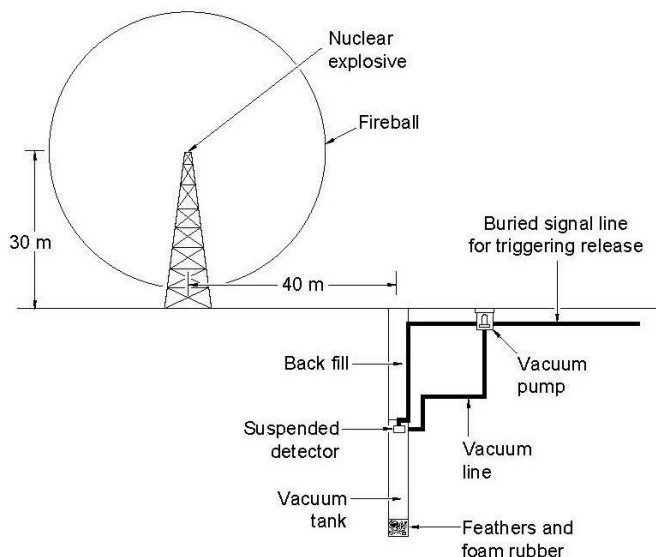
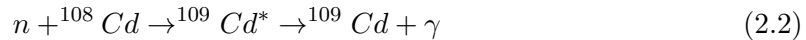


Figure 2.1: Original sketch of Cowan and Reines first proposed neutrino experiment.

Later, Reines realized tagging both the positron and neutron through a double coincidence would drastically reduce the backgrounds. This meant they could use a less intense neutrino source such as a nuclear reactor. They chose the Savannah River Plant near Augusta, Georgia which was estimated to produce neutrino fluxes on the order of $10^{12} - 10^{13}$ neutrinos/s/cm². The detector was composed of a water target that was doped with CdCl₂. As stated prior, the signal would rely on a double coincidence flash measured from photomultipiler tubes inside their detector. First, they would detect the positron as it annihilates with an electron via pair production ($e^+ + e^- \rightarrow \gamma + \gamma$). This is identified by two, back-to-back, coincident 0.511 MeV photons. Then, approximately 5μS later, a secondary photon would be detected which was produced from the neutron capture on Cadmium as shown in equation 2.2.



In 1956, only 25 years after Pauli's initial proposal of the neutrino, Cowan and Reines succeeded and provided the first direct experimental evidence of the electron flavor neutrino. In the subsequent years, the existence of two other flavors of neutrinos have been verified. In 1962, Lederman, Schwartz, and Steinberger discovered the ν_μ at Brookhaven Nation Laboratory by measuring neutrinos coming from pion decay. The ν_μ would be distinctly different from that of ν_e if the process $\nu_\mu + n \rightarrow p + e^-$ was forbidden. The results showed that the neutrinos from pion decay were indeed muon-like. Finally in 2000, the DONUT(Direct Observation of NeUtrino Tau) experiment stationed at Fermilab, made the first observed measurement of the ν_τ .

In 1956, C.S. Wu had shown that outgoing electron from beta decay maintained an opposing spin with respect to the spin of the parent nucleus. This turned out to be the first proof of maximal parity violation in weak interactions. Shortly thereafter, the neutrino helicity was first measured at Brookhaven National Labs by Maurice Goldhaber. In nature, neutrinos only have left handed helicity, while anti-neutrinos have right handed helicity. Helicity is frame dependent for particles with mass, which means there can be a reference frame in which the momentum vector can switch but the spin vector will not. For a

203 mass zero particles, this is not possible because the particle would already be traveling at
 204 the speed of light. This assumption is what lead to the believe that neutrinos were massless.

205 The number of active light neutrinos are well constrained by studying the decay of the
 206 Z^0 boson at LEP(Large Electron-Positron collider). LEP was an electron-positron collider
 207 ring with a circumference of approximately 27 km that supported four primary experiments
 208 (L3, ALEPH, OPAL and DELPHI). The facility was coined the phrase “Z-Factory” due
 209 to it’s ability to record approximately 1000 Z^0 boson decays every hour during optimal
 210 running conditions. The number of active neutrinos, N_ν is related to the width of the Z^0
 211 resonance. Using 17 million Z^0 decays, LEP was able to show that $N_\nu = 2.9840 \pm 0.0082$

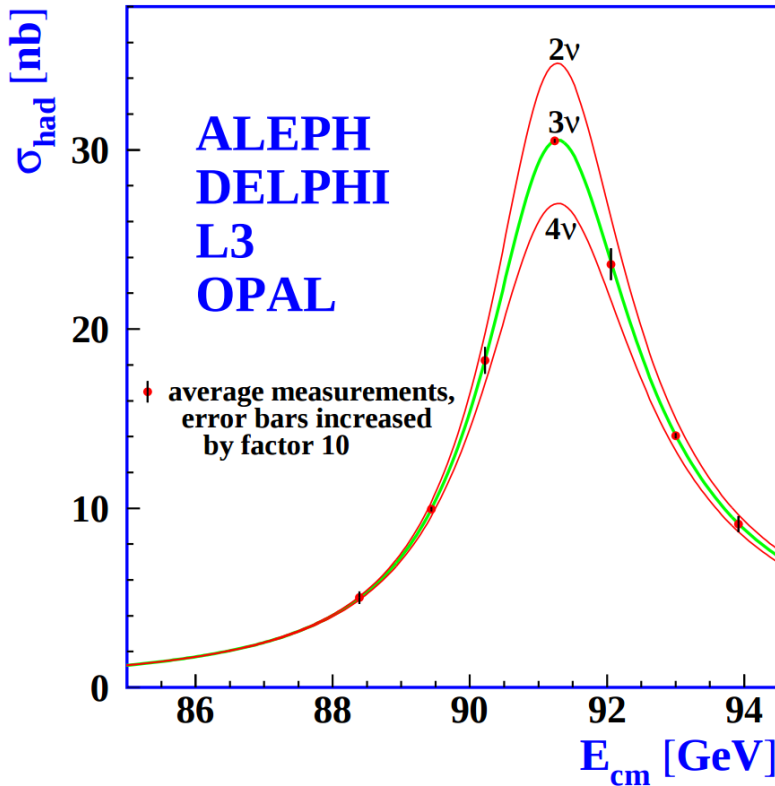


Figure 2.2: The Hadron production cross section around the Z^0 resonance from LEP. The curves for two, three, and four neutrino flavors are shown. The fit shows very compelling evidence of three active flavors of neutrinos.

212 2.3 Neutrinos in the Standard Model

213 In the later half of the 20th century, scientists were looking for a way to describe all the
214 fundamental forces and classify the known particles. The standard model of particle physics
215 is a phenomenological framework that describes the interaction of fundamental particles be-
216 tween the strong and electroweak forces. Having stood the test of time, the standard model
217 accurately predicts most elementary particle interactions, but, does have it's limitations.
218 The standard model does not account for gravity nor does it account for many new physics
219 issues such as dark matter or dark energy. Most importantly, as we will see in section 2.5,
220 it does not provide an accurate description of the neutrino.

221 The standard model consists of two types of particles, bosons and fermions. The funda-
222 mental bosons consist of two families: gauge bosons, which are typically the force carriers,
223 and scalar bosons, which refer to spin zero particles or fields. The gluon, photon, and the
224 weak boson are gauge bosons that mediate the strong, electromagnetic, and weak forces,
225 respectively. The Higgs boson is a scalar boson that possesses a nonzero vacuum expec-
226 tation value of 246GeV . This provides a mechanism for certain particles to gain mass
227 even though their symmetries would suggest zero mass. The fundamental fermions are also
228 divided into two families, quarks and leptons each having three generations. The quarks
229 compose two main categories of particles, baryons and mesons. Baryons consist of an en-
230 semble of 3 quarks. The most common and stable baryons in the universe are protons(uud)
231 and neutrons(udd). Meson consist of an ensemble of quark anti-quark pairs and tend to
232 have shorter lifetimes than their corresponding baryons. The lightest and most common
233 mesons are pions($u\bar{d}, d\bar{u}, u\bar{u}/d\bar{d}$) and kaons($u\bar{s}, s\bar{u}, d\bar{s}/s\bar{d}$). The leptons are also divided into
234 two families with three generations each. The charged leptons, most notably the electron,
235 interact via the strong and weak nuclear force and combine to form common baryonic mat-
236 ter. The neutral leptons are the neutrinos and only interact via the weak nuclear force.
237 More details such as, mass, charge, and spin for various particles are shown in figure 2.3

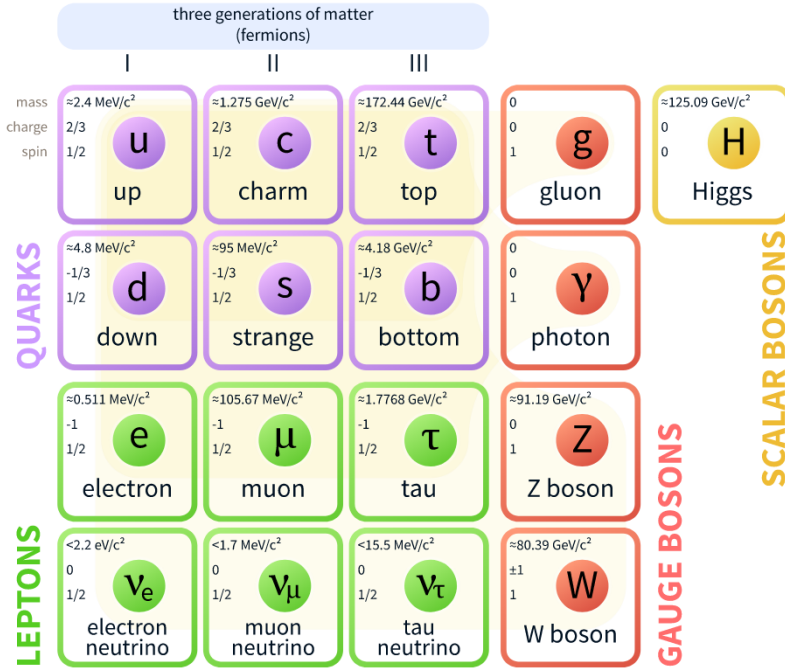


Figure 2.3: The current view of the standard model.

²³⁸ 2.4 Neutrino Interactions

²³⁹ Neutrinos interact via the weak force. In the standard model, the weak force is unified
²⁴⁰ with the electromagnetic force through an $SU(2) \otimes U(1)$ symmetry. The structure of the
²⁴¹ $SU(2)$ group symmetry accounts for the chirality of the fermion fields, along with ability to
²⁴² produce massive gauge bosons. The $U(1)$ group symmetry accounts for the massless photon
²⁴³ propagator needed for electromagnetic interactions. For the quark and fermion families we
²⁴⁴ define fermion fields in equations 2.3 and 2.4 , respectively. For formality we will define
²⁴⁵ right(left)- handed neutrino(anti-neutrino) fields knowing that they will become irrelevant
²⁴⁶ as the theory evolves:

$$\psi_1(x) = \begin{pmatrix} q \\ q' \end{pmatrix}_L , \quad \psi_2 = q_R , \quad \psi_3 = q'_R \quad (2.3)$$

$$\psi_1(x) = \begin{pmatrix} \nu \\ l \end{pmatrix}_L , \quad \psi_2 = \nu_R , \quad \psi_3 = l_R \quad (2.4)$$

247 We begin with the free Lagrangian, defined in equation 2.5, as it is already invariant in
248 flavor space.

$$\mathcal{L}_{\text{free}} \equiv \bar{\psi}(i\cancel{\partial} - m)\psi = i\bar{\psi}(x)\gamma^\mu\partial_\mu\psi(x) - m\bar{\psi}(x)\psi(x) \quad (2.5)$$

249 To make the Lagrangian invariant under local $SU(2) \otimes U(1)$, the fermion derivatives
250 have to be changed to covariant objects. This produces 4 different gauge parameters, shown
251 in equations 2.6, which correspond to the 4 different gauge fields required to describe the
252 W^\pm , Z^0 , and γ .

$$\begin{aligned} D_\mu\psi_1(x) &\equiv [\partial_\mu - ig\widetilde{W}_\mu(x) - ig'y_1B_\mu(x)]\psi_1(x) \\ D_\mu\psi_2(x) &\equiv [\partial_\mu - ig'y_2B_\mu(x)]\psi_2(x) \\ D_\mu\psi_3(x) &\equiv [\partial_\mu - ig'y_3B_\mu(x)]\psi_3(x) \end{aligned} \quad (2.6)$$

253 Where, σ^i are the Pauli spin matrices and B_μ represents a field imposed by an external
254 source. We find that,

$$\begin{aligned} \widetilde{W}_\mu(x) &\equiv \frac{\sigma_i}{2} \left\{ \partial_\mu W_\nu^i - \partial_\nu^i + g\epsilon^{ijk}W_\mu^jW_\nu^k \right\} \\ B_{\mu\nu} &\equiv \partial_\mu B_\nu - \partial_\nu B_\mu \end{aligned} \quad (2.7)$$

255 The Lagrangian now satisfies $SU(2) \otimes U(1)$ symmetry between all gauge fields as shown
256 in equation 2.8. It should be noted that the fermion fields and gauge bosons are required to
257 be massless. This does not accurately describe the true interaction since 3 of the 4 gauge
258 bosons are known to have mass, but the theory does allow an interface between neutrino
259 interactions in the standard model.

$$\mathcal{L} = \sum_{j=0}^3 i\bar{\psi}_j(x)\gamma^\mu D_\mu\psi_j(x) \quad (2.8)$$

260 From equation 2.8, the terms that account for interaction of gauge bosons with the
261 fermion fields are shown below in equation 2.9

$$\mathcal{L} \rightarrow g\bar{\psi}_1(x)\gamma^\mu\widetilde{W}_\mu\psi_1(x) + g'B_\mu\sum_{j=0}^3 y_j\bar{\psi}_j(x)\gamma^\mu\psi_j(x) \quad (2.9)$$

262 From this, we are then able to construct the Lagrangian for both the charged and neutral
 263 currents. The charge current Lagrangian is shown in equation 2.10.

$$\mathcal{L}_{CC} = \frac{g}{2\sqrt{2}} \left\{ W_\mu^\dagger [\bar{q}\gamma^\mu(1-\gamma_5)q' + \bar{\nu}\gamma^\mu(1-\gamma_5)\bar{l}] + \dots \right\} \quad (2.10)$$

264 The neutral current term in the Lagrangian contains gauge fields for both the Z boson
 265 and photon, which can be broken into two terms to account for a non-zero Z boson mass
 266 while leaving the photon massless through spontaneous symmetry breaking(SSB). This is
 267 done through an arbitrary rotation, as shown in equation 2.11, where θ_w is known as the
 268 Weinberg or weak mixing angle. This angle is important because it is the angle used to
 269 rotate through SSB giving the Z boson its mass.

$$\begin{pmatrix} W_\mu^3 \\ B_\mu \end{pmatrix} = \begin{pmatrix} \cos \theta_w & \sin \theta_w \\ -\sin \theta_w & \cos \theta_w \end{pmatrix} \times \begin{pmatrix} Z_\mu \\ A_\mu \end{pmatrix} \quad (2.11)$$

270 It is then possible to write the neutral current Lagrangian that accounts for the inter-
 271 action of the Z boson as shown in equation 2.13.

$$\mathcal{L}_{NC} = \frac{e}{2\sin(\theta_w)\cos(\theta_w)} Z_\mu \sum_f \bar{f}\gamma^\mu(v_f - \alpha_f\gamma_5)f \quad (2.12)$$

272 where,

$$g\sin(\theta_w) = g'\cos(\theta_w) = e \quad \text{and} \quad \cos(\theta_w) = \frac{M_w}{M_z} \quad (2.13)$$

273 The neutral current coupling constants, v_f & α_f , differ with respect to the various quark,
 274 charged and neutral lepton fields. The neutrinos can be described as interactions via the
 275 charged and neutral currents. The Feynman diagrams, shown in figure 2.4, depict how the
 276 leptons couple to the quarks via the current mediator.

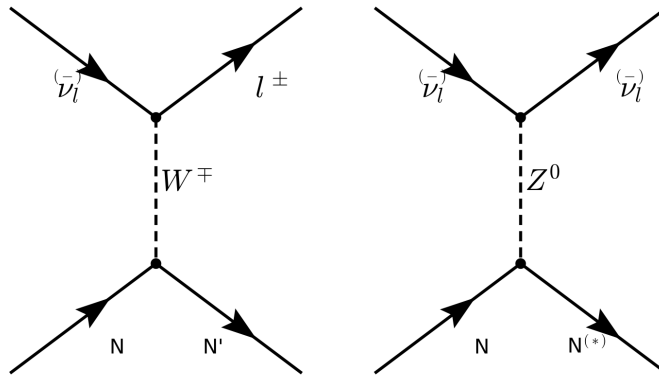


Figure 2.4: The Feynman diagram on the left describes a charged current(CC) neutrino interaction which transforms neutrinos into their corresponding charged leptons. In the CC interaction diagram the $N \rightarrow N'$ represents a changed nucleon charge. The diagram on the right shows the neutral current(NC) neutrino interaction with preserves the neutrino while it interacts. In the NC interaction diagram the $N \rightarrow N^*$ represents a same charge nucleon that could be at a higher resonance state.

2.5 Neutrino Mass and Flavor Oscillations

Neutrino oscillation is a quantum mechanical phenomenon in which the fraction of neutrino flavor changes while it propagates. This phenomena was first proposed in 1957 by Bruno Pontecorvo and relates the neutrino mass eigenstates with the flavor eigenstates through a rotation. This phenomena is best shown through a two neutrino flavor example, then extended into 3 flavors.

The mixing matrix for a two flavor neutrino case is:

$$\begin{pmatrix} \nu_e \\ \nu_\mu \end{pmatrix} = \begin{pmatrix} \cos \theta & \sin \theta \\ -\sin \theta & \cos \theta \end{pmatrix} \begin{pmatrix} \nu_1 \\ \nu_2 \end{pmatrix} \quad (2.14)$$

In this example, the flavor states are represented as ν_e and ν_μ which are expressed as a mixture of mass states ν_1 and ν_2 . For ascetic reasons, we chose ν_μ to be part of the example because most man made neutrino beams produce a relative pure sample of ν_μ . The framework for this example is commonly used as an oscillation approximation and can be generalized to satisfy any case of two distinctly different flavor neutrinos.

289 Using the two flavor formalism a pure ν_μ neutrino state can be expressed as equation
 290 2.15

$$|\nu_\mu(0)\rangle = -\sin \theta |\nu_1(0)\rangle + \cos \theta |\nu_2(0)\rangle \quad (2.15)$$

291 The evolution of the state is governed by solving the time dependent Schroedinger
 292 equation for the initial muon state:

$$|\nu_\mu(t)\rangle = e^{-i\frac{Et}{\hbar}} |\psi(0)\rangle = -e^{-i\frac{E_1 t}{\hbar}} \sin \theta |\nu_1\rangle + e^{-i\frac{E_2 t}{\hbar}} \cos \theta |\nu_2\rangle \quad (2.16)$$

293 Assuming neutrinos travel near the speed of light, we rewrite equation 2.16 using the
 294 relativistic approximation, along with setting $c = \hbar = 1$ and $p_1 = p_2 = p$:

$$|\nu_\mu(t)\rangle \simeq -e^{-i(p_1 + \frac{m_1^2}{2p_1})t} \sin \theta |\nu_1\rangle + e^{-i(p_2 + \frac{m_2^2}{2p_2})t} \cos \theta |\nu_2\rangle \quad (2.17)$$

295 with,

$$E = \sqrt{p^2 + m^2} = p \sqrt{1 + \frac{m^2}{p^2}} \approx p + \frac{m^2}{2p} \quad (2.18)$$

296 Next, the mass terms are grouped together and defined as the absolute square difference,
 297 $\Delta m^2 \equiv |m_2^2 - m_1^2|$. We find that if the mass are different then the mass eigenstates propagate
 298 at different frequencies and give rise the oscillatory behavior. The time dependent state can
 299 now be wrote as:

$$|\nu_\mu(t)\rangle = e^{-i\phi} (-\sin \theta |\nu_1\rangle + e^{+i\frac{\Delta m^2}{2p}t} \cos \theta |\nu_2\rangle) \quad (2.19)$$

with, $e^{-i\phi} \equiv e^{-i\left(p + \frac{m_1}{2p}\right)t}$

300 To calculate the probability of the initial ν_μ state being measured as a ν_e state at some
 301 later time t , we need to calculate the absolute value squared of the overlap between the
 302 states. Utilizing the relationship $\langle \psi_i | \psi_j \rangle = \delta_{i,j}$, the overlap between the states is:

$$\langle \nu_e | \nu_\mu(t) \rangle = e^{-i\phi} (-\sin \theta \cos \theta + \sin \theta \cos \theta e^{i\frac{\Delta m^2}{2p}t}) \quad (2.20)$$

303 The probability reduces to:

$$\begin{aligned}
 P(\nu_\mu \rightarrow \nu_e) &= |\langle \nu_e | \nu_\mu(t) \rangle|^2 \\
 &= e^{i\phi} e^{-i\phi} \sin^2 \theta \cos^2 \theta (-1 + e^{-i\frac{\Delta m^2}{p}t})(-1 + e^{+i\frac{\Delta m^2}{p}t}) \\
 &= \frac{1}{2} \sin^2 2\theta \left(1 - \cos \left(\frac{\Delta m^2}{2p} t \right) \right)
 \end{aligned} \tag{2.21}$$

304 Finally, from relativistic assumptions, we set $p = E_\nu$ as the outgoing neutrino energy
 305 and $t = L$ corresponds to the distance traveled.

$$P(\nu_\mu \rightarrow \nu_e) = \sin^2 2\theta \sin^2 \left(\frac{\Delta m^2 L}{4E_\nu} \right) \tag{2.22}$$

306 From a proper accounting of numerical values of c and \hbar , equation 2.26 is more com-
 307 monly written as:

$$P(\nu_\mu \rightarrow \nu_e) = \sin^2 2\theta \sin^2 \left(1.27 \frac{\Delta m^2 L}{E_\nu} \right) \tag{2.23}$$

308 This oscillation behavior is best visualized as a plot of the probability of appearance
 309 and disappearance as shown Figure 2.5.

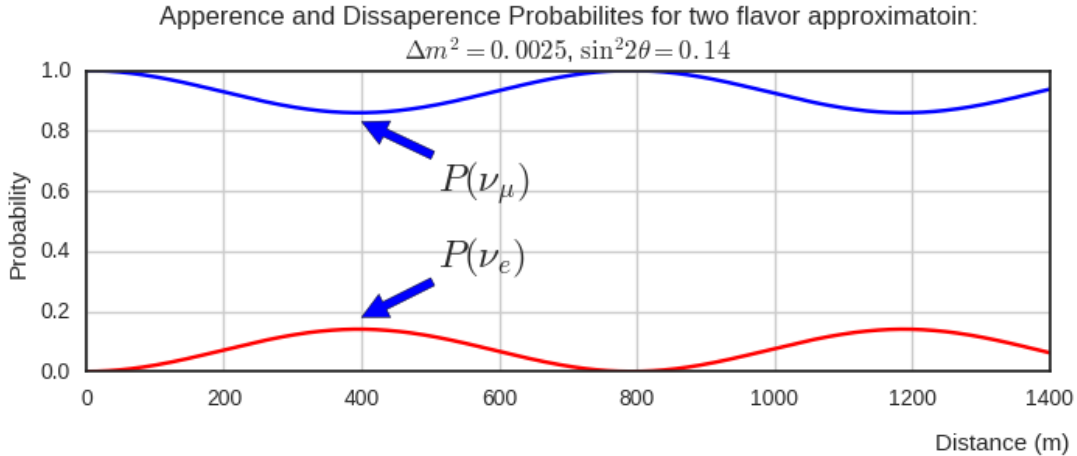


Figure 2.5: This plot shows the appearance and disappearance curves for a 2-flavor approximation as a function of baseline. The values of $\Delta m^2 = 0.0025 \text{ eV}^2$ and $\sin^2 \theta = 0.14$ are used.

As shown prior from figure 2.2, there are very good constraints on the number of active neutrinos. Extending this formalism to a 3 flavor case was done by Pontecorvo-Maki-Nakagawa-Sakata (PMNS). The PMNS matrix is a 3 dimensional unitary matrix which is parameterized by three mixing angles $\theta_{12}, \theta_{23}, \theta_{13}$ a complex phase δ . The three angle correspond to the mixing effect, while δ is known as the charge parity(CP) phase. If the CP-phase is non-zero, then neutrinos violate charge parity conservation which leads to the conclusion that neutrinos and anti-neutrinos interact differently with matter. The value for δ has yet to be observed.

$$U_{PMNS} = \begin{pmatrix} 1 & 0 & 0 \\ 0 & c(\theta_{23}) & s(\theta_{23}) \\ 0 & -s(\theta_{23}) & c(\theta_{23}) \end{pmatrix} \begin{pmatrix} c(\theta_{13}) & 0 & s(\theta_{13})e^{-i\delta} \\ 0 & 1 & 0 \\ -s(\theta_{13})e^{i\delta} & 0 & c(\theta_{13}) \end{pmatrix} \begin{pmatrix} c(\theta_{12}) & s(\theta_{12}) & 0 \\ -s(\theta_{12}) & c(\theta_{12}) & 0 \\ 0 & 0 & 1 \end{pmatrix} \quad (2.24)$$

where $c(\theta_{ij}) \equiv \cos \theta_{ij}$ and $s(\theta_{ij}) \equiv \sin \theta_{ij}$. The matrix equation is now put into a more compact manor that relates the mixing of the 3 neutrino generations.

$$\begin{pmatrix} \nu_e \\ \nu_\mu \\ \nu_\tau \end{pmatrix} = \begin{pmatrix} U_{e,1} & U_{e,2} & U_{e,3} \\ U_{\mu,1} & U_{\mu,2} & U_{\mu,3} \\ U_{\tau,1} & U_{\tau,2} & U_{\tau,3} \end{pmatrix} \begin{pmatrix} \nu_1 \\ \nu_2 \\ \nu_3 \end{pmatrix} \quad (2.25)$$

In it's most general form, the oscillation probability is:

$$P(\nu_\alpha \rightarrow \nu_\beta) = \delta_{\alpha,\beta} - 4 \sum_{j>i} U_{\alpha,i} U_{\beta,i} U_{\alpha,j}^* U_{\beta,j}^* \sin^2 \left(1.27 \frac{\Delta m_{ij}^2 L}{E_\nu} \right) \quad (2.26)$$

From equation 2.26, we see that the oscillation probability is depended on the mass difference between states. There is currently no method to directly measure the mass of any given neutrino. Therefore, there is an allowed ambiguity in the mass ordering of all three neutrino states. This is called the neutrino hierarchy problem. However, we do know that the difference between m_1 and m_2 is small relative to m_3 . Using this, we can build a picture of the fraction of different flavor eigenstates corresponding to their various mass states for both types of hierarchy.

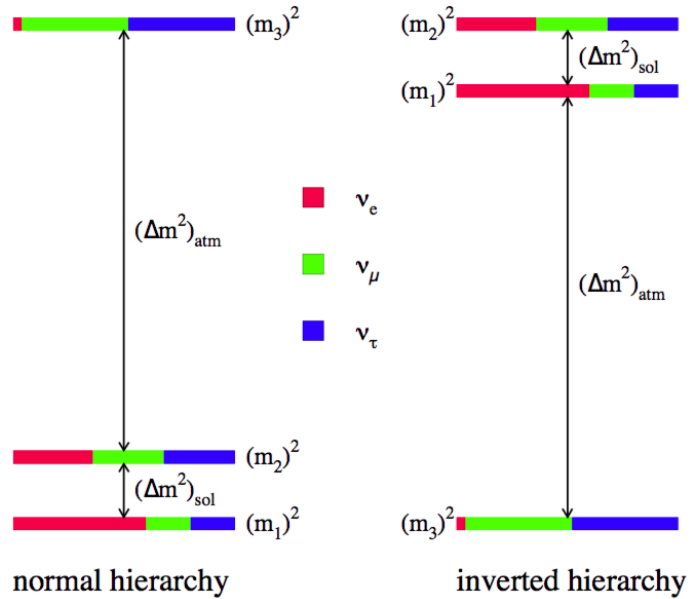


Figure 2.6: The two possible ordering for the 3 active neutrino mass eigenstates.

Many experiments have measured various elements of the PMNS matrix with neutrinos coming from accelerators, reactors, and solar sources. Currently, normal hierarchy ($m_1 < m_2 < m_3$) is favored, therefore we will show (table 2.27) the current Particle Data Group(PDG)] best fit values for oscillation parameters with respect to normal hierarchy.

$$\begin{aligned}
\Delta m_{21}^2 &= 7.37 \times 10^{-5} eV^2 \\
\Delta m_{32}^2 &= 2.50 \times 10^{-3} eV^2 \\
\sin(\theta_{12}) &= 0.297 \\
\sin(\theta_{23}) &= 0.437 \\
\sin(\theta_{13}) &= 0.0214 \\
\delta/4 &= 1.35
\end{aligned} \tag{2.27}$$

³³² **2.6 Sterile Neutrinos**

³³³ It is well accepted, from measurements at LEP[], that there are only 3 neutrinos that couple
³³⁴ through the weak interaction. Mathematically, nothing prohibits a theory that allows for
³³⁵ neutrino mixing with other neutrino states beyond the 3 active states. These states, since
³³⁶ they do not interact weakly, are called 'sterile neutrinos'. Extending the 3 flavor oscillation
³³⁷ model to include any number of sterile neutrinos may be a possibility to address some the
³³⁸ currently unexplained results in the neutrino physics fields. Each additional state requires
³³⁹ an extra dimension to be added to the PMNS matrix. The sterile eigenstates are then
³⁴⁰ defined as

$$|\nu_{s_i}\rangle = \sum_j^{3+N} U_{s_i,j} |\nu_j\rangle \quad (2.28)$$

³⁴¹ where N is the number of sterile neutrinos. The necessity for additional sterile neutrinos
³⁴² was prompted by the LSND experiment and later supported by the MiniBooNE. experiment.
³⁴³ Both experiments are explained in depth in chapter 5. Each experiment found an excess
³⁴⁴ of electron-like events at low energy. This suggested a Δm^2 parameter space observed to
³⁴⁵ be 1eV^2 larger than expected and strongly contradicted the results of many other results
³⁴⁶ which had Δm^2 around $\mathcal{O}(10^{-3}\text{eV}^2)$ and $\mathcal{O}(10^{-5}\text{eV}^2)$. This precipitated the need for
³⁴⁷ further exploration of the LSND and MiniBooNE claims with more sophisticated detector
³⁴⁸ technologies. The MicroBooNE experiment was proposed in 2007¹ and will be the focal
³⁴⁹ point for this thesis.

350 Chapter 3

351 The MicroBooNE Detector

352 3.1 Brief History of LAr-TPC's

353 The surprising nature of neutrinos quickly prompted the need for precision measurements
354 of their interactions. Unfortunately, the low neutrino cross section posed a hurdle to build
355 a high statistics detector. In 1977, C.Rubbia propose a Liquid Argon Time Projection
356 Chamber (LArTPC) as large, high precision neutrino detector.^[1] In 2001, The ICARUS col-
357 laboration commissioned the T600 detector which was one of the first large scale LArTPC's
358 to be used as a neutrino detector. ^[2] The T600, which is comprised 760 tons of liquid argon
359 and commissioned in Pavia, Italy using cosmic rays as a proof of principle. Later the T600
360 was place underground in Hall B of Laboratori Nazionali del Gran Sasso (LNGS) which is
361 located 730 km from the source of the CERN neutrino beam.

362 In 2009, the AgroNeut collaboration, commissioned a small LArTPC in a 175 liter
363 vacuum jacketed cryostat. The ArgoNeut TPC was comprised of 3 wire planes and operated
364 at a drift field of 500 V/cm. The detector was placed just in front of the MINOS near
365 detector in the NuMI beam at Fermi National Accelerator Laboratory(FNAL)^[3]. AgroNeut
366 collected thousands of neutrino and antineutrino events providing valuable physics data and
367 detector R&D for future experiments with LArTPC's.

368 The MicroBooNE (the Micro Booster Neutrino Experiment) detector, which will be
369 discussed in depth throughout this chapter, is the first multi-ton LArTPC to be fully op-
370 erational in the U.S. The MircoBooNE detector design pioneered many new detector R&D

371 concepts such as: the ability to maintain high LAr purity in an unevaluated vessel, imple-
 372 mentation of low noise electronic readouts at liquid cryogenic temperatures and advances
 373 in reconstruction techniques. MicroBooNE also, supports a robust, high statistics physics
 374 program to address the MiniBooNE Low Energy Excess and various cross section measure-
 375 ments. MicroBooNE was commissioned and began taking cosmic ray data in the summer of
 376 2015. In October 2015 it began taking neutrino data. Shortly there after, the first neutrino
 377 event candidates were identified. []

378 **3.2 Introduction**

379 The MicroBooNE detector utilizes 170 tons of liquid argon to sustain 87 tons of active
 380 detector mass. It is located at the Liquid Argon Test Facility (LARTF) which is 470
 381 m downstream of the Booster Neutrino Beam-line(BNB) source at the Fermilab National
 382 Accelerator Lab (FNAL) in Batavia, Illinois. The detector is the first large scale LArTPC
 383 to be deployed, commissioned and fully operated in the US.

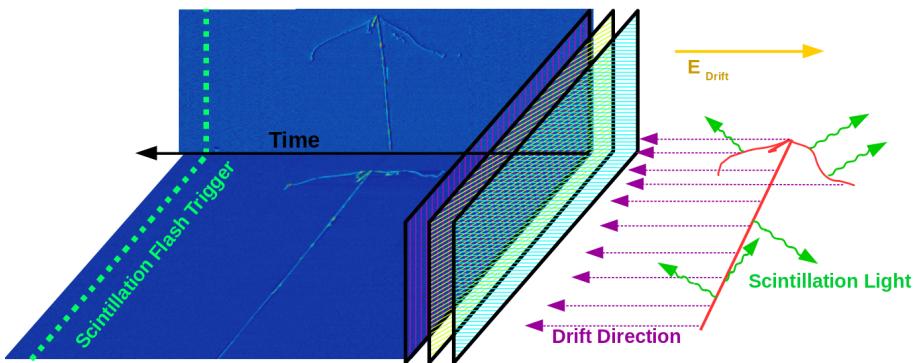


Figure 3.1: This diagram explains how a TPC works. First, charged tracks ionize the argon. The remaining ions produce prompt scintillation light and the corresponding electrons begin to drift towards the wires due to the presence of the electric field. When the drift electrons reach the wire planes a 2D image is produced for each plane. When combining the 2D images from multiple planes along with the scintillation light information a 3D reconstruction is possible.

384 The general principle of a LArTPC involves utilizing two properties of LAr, scintillation

385 light and ionization. Charged particles travel through the argon and produce scintillation
386 light which is collected by photomultiplier tubes (PMT's). A uniform electric field is applied
387 over active volume which transports the ionization electrons to a series of wire planes.
388 Assuming the argon is pure and has minimal electro-negative contaminants, the wire planes
389 then measure the induced or collected charge signal from the drifting electrons. The planes
390 are each oriented at a different pitch angles. Each plane then can then produce a two
391 dimensional image of the event as a function of wire and time. Combining multiple planes
392 along with the PMT information allows for the object to be fully reconstructed in three
393 dimensions. A diagram of the TPC concept is show in Figure 3.1. In the following sections
394 the TPC, light collection system, and electronics are described in detail.

395 **3.3 Time Projection Chamber**

396 The TPC is the core of the MicroBooNE detector and forms a rectangular prism with
397 dimensions $2.3m \times 2.6m \times 10.4m$ which contains 87t of LAr. The longest dimension, which
398 in MicroBooNE's coordinate system is refereed to as the z-direction, is oriented on axis
399 of the BNB. The majority of the TPC materials are composed of 304V stainless steel
400 and G10. Stainless steel was chosen due to it's low magnetic susceptibility, resistance to
401 corrosion/oxidation, and ability to maintain it's strength in cryogenic temperatures. G10
402 was chosen due to it's ability to perform well as an insulator in cryogenic environments.



Figure 3.2: The MicroBooNE TPC is shown here. On the far right is the flat cathode plane. The far left shows the 8,456 anode wires installed. The field cage tubes, which provide the uniform electric field, span the length between the anode and cathode.

403 The TPC field cage, which provides the uniform electric field through the detector
 404 volume, and was designed to produce field strengths up to 500 v/cm in liquid argon. The
 405 field cage consists of a total of 64 stainless steel rectangular loops that are supported and
 406 evenly spaced by a G10 holder. The cathode plane is a series flat stainless steel sheets that
 407 is opposite the anode sense wires. Figure 3.2 shows the MicroBooNE TPC.

408 Every piece that was used in the MicroBooNE detector was thoroughly cleaned. Many
 409 pieces were cleaned in an ultrasonic cleansing bath while others were cleaned by hand.
 410 The detector was constructed in a clean environment that maintained positive pressure to
 411 mitigate the accumulation of dust. A complete description of the process is summarize in
 412 a separate technical note. []

413 MicroBooNE has a total of 8,265 sense wires that form 3 unique wire planes, one vertical
 414 collection plane (Y) and two induction planes (U,V) oriented at ± 60 relative the Y plane.
 415 The wire planes are separated by 3 mm. The wires in each plane are evenly spaced by 3
 416 mm pitch on carrier boards. The Y plane consists of 3,456 wires with a total of 108 carrier
 417 boards that accommodate 32 wires each. Each of the U and V planes consist of 2,400 wires
 418 with a total of 150 carrier boards that accommodate 16 wires each. The wires themselves
 419 are made of 304V stainless steel and are $150 \pm 5\mu\text{m}$ in diameter. A $2\mu\text{m}$ layer of copper
 420 is plated over the wires to decrease the resistivity from $40\Omega/\text{m}$ to $3\Omega/\text{m}$. The reduced

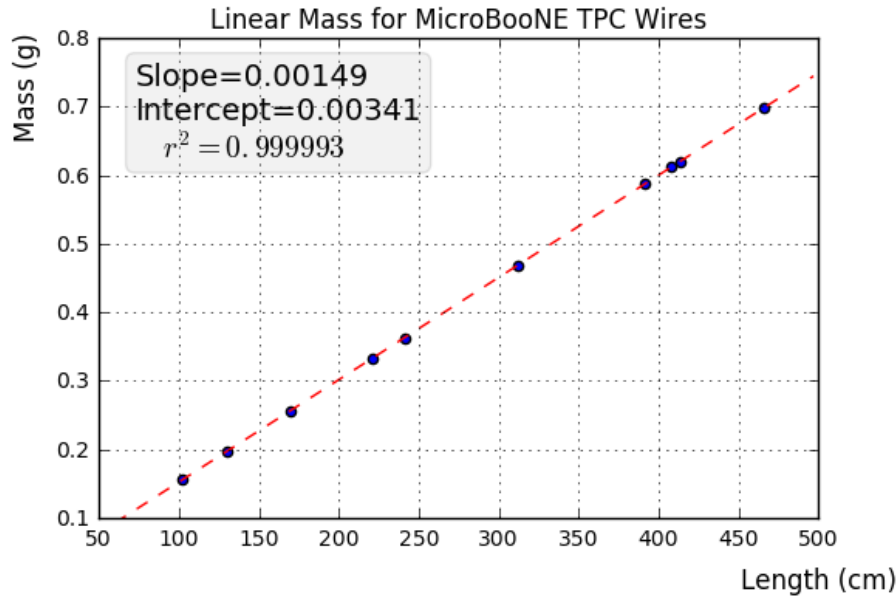


Figure 3.3: This plot is for a small sample used to cross check the linear mass density measured from the wire dealer. The slope from this plot represents the linear mass density and was found to be consistent with the value 0.149g/m

421 resistivity aids in noise reduction at cryogen temperatures. Finally the wire is covered in
 422 and outer layer 0.1 μ m of gold to prevent the copper from oxidizing over time. The linear
 423 mass density of a small sample of wires was measured and is shown in figure 3.3.

424 The wires were designed to installed at a nominal tension of 6.97 N. To account for this,
 425 the carrier boards were installed onto a series of tensioning bars on the anode frame. These
 426 tensioning system, as shown in figure 3.4, allowed for fine tune adjustments to be made to
 427 separate sections of wires.

428 There are a total of 12 tensioning bars, 2 sets of 5 that traverse the entire top and bottom
 429 length of the anode frame, and 2 spanning the entire height of the upstream and downstream
 430 sections of the anode frame. Bronze jacking screws were used for final adjustments once
 431 all the wires were installed. Bronze was chosen since it has a similar thermal expansion
 432 coefficient to stainless steel and it is a softer metal which helps mitigate the risk of cold
 433 welding with stainless steel during the tensioning process.

434 In preparation for installing the actual detector wires, an installation team was trained

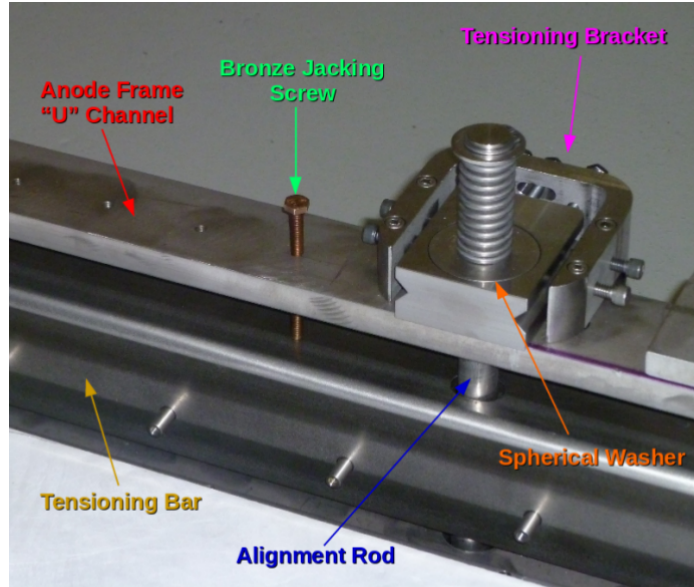


Figure 3.4: The MicroBooNE tension system. Wire carrier boards (not shown here) are mounted on the tensioning bar. The tensioning bar is able to move the wires during the tensioning process. Bronze jacking screws were used for final alignment during the tensioning process

435 on how to properly handle and install them. A 'mock-wire' installation was done to practice
 436 and identify the risks. After this, the actual wires were installed. The installation took
 437 approximately one week. The wires were installed serially, first the Y-plane, then the U-
 438 plane, and then the V-plane. After all the wires were install, a G10 cover board was placed
 439 over carrier boards to secure and protect the electronics on the board, as shown in figure
 440 3.5.

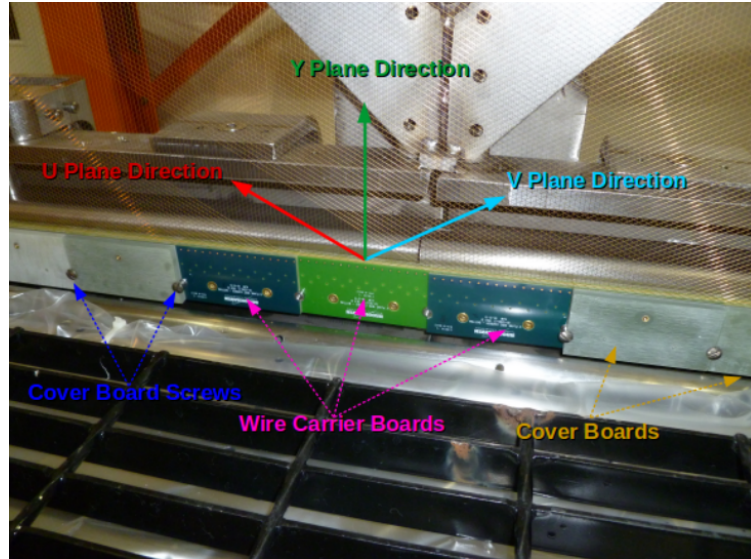


Figure 3.5: The MicroBooNE wires for 3 planes are shown here. The wire carrier boards are serially installed on the tensioning bar. The boards are held in place with a G10 cover plate that is secured with a smooth stainless steel screw.

441 Next, the wires were brought as close to nominal tension as possible. It was decided to
 442 favor under tensioning wires to minimize the risk of a broken wire during the tensioning
 443 process. The wire tensioning was done in a systematic way using the bronze jacking screws.

$$f = \frac{1}{2L} \sqrt{\frac{T}{\rho}} \quad (3.1)$$

444 Each wire has a characteristic resonance frequency that is related to its length, tension,
 445 and linear mass density through equation 3.1. A custom device was made to measure
 446 the resonant frequency of individual MicroBooNE wires. A laser light was focused on a
 447 particular wire and the wire gently plucked. A photo-diode mounted in an optical lens then
 448 measured the intensity of reflected light as the wire vibrated. The signals were then read into
 449 SpectrumAnalyzer, which is a software package that records frequency. SpectrumAnalyzer
 450 also allowed the high order frequency harmonics to be seen. The higher frequencies allowed
 451 for more precise tension measurement as see in Figure 3.6

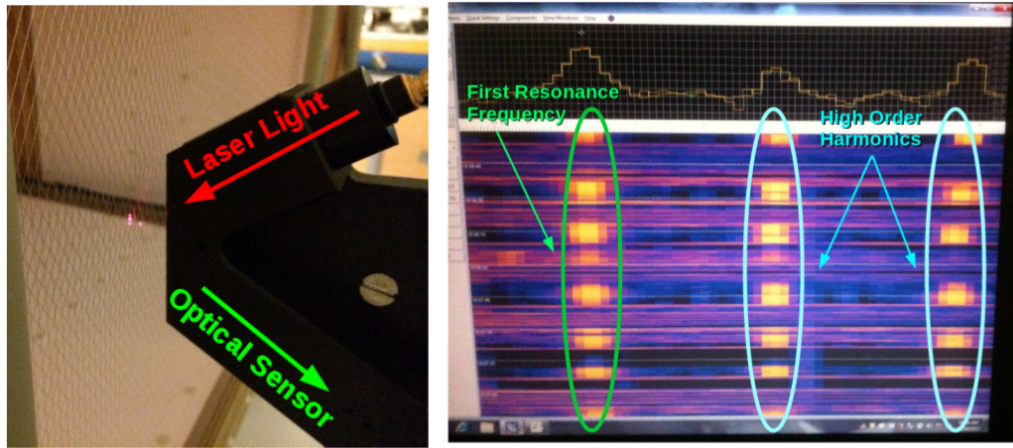


Figure 3.6: Left: Picture of the tension measuring apparatus including a laser and a optical sensor made of a photo-diode and a lens. Right: Example output of the SpectrumAnalyzer showing the first resonance frequency (bright line on the left) and the higher order harmonics (lines in the middle and left).

452 Note that the tension of 2328 out of 2400 U wires, 2308 out of 2400 V wires, and 3410
 453 out of 3456 Y wires was measured, corresponding to 97.5 % of all wires installed in the
 454 detector. Only the wires inaccessible to the tension measuring device were not measured.
 455 The average tension for U,V,Y planes respectively was 0.589 ± 0.012 kg, 0.664 ± 0.014 kg,
 456 0.525 ± 0.009 kg. The tension for each plane is shown in Figure 3.7 and Figure 3.8.

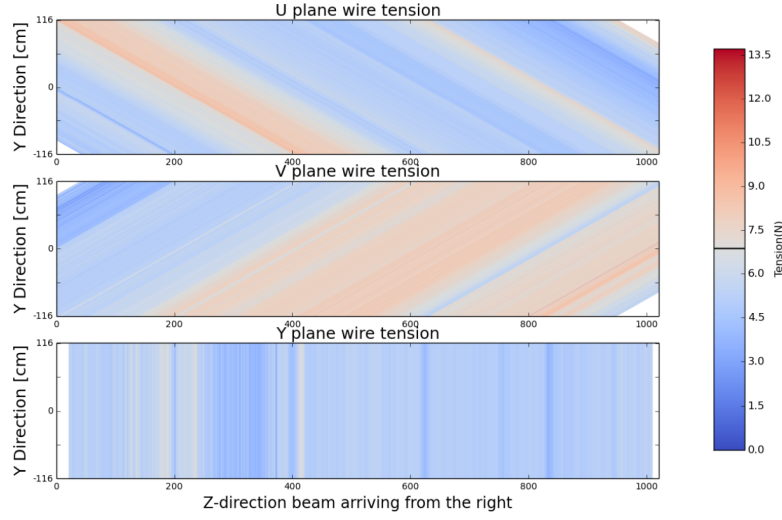


Figure 3.7: This a plane by plane map of the measured wire tensions for MicroBooNE.

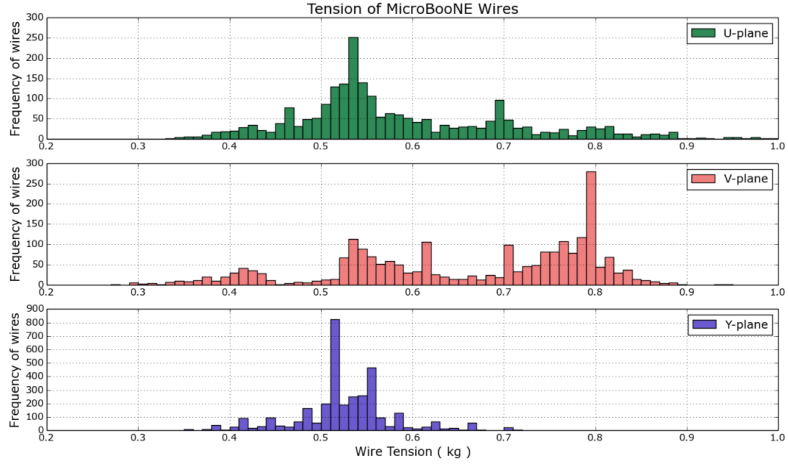


Figure 3.8: This a plane by plane histogram of the measured wire tensions for MicroBooNE.

3.4 Light Collection

The TPC can reconstruct 3D objects but there is still an ambiguity in the initial drift position. The light collection system in an LArTPC provides information to address this degeneracy. Scintillation light of liquid argon is 128nm wavelength and is produced through two primary reactions. The first, which accounts for $\approx 25\%$ of the light yield, is done through a Σ singlet excimer excitation and has a reaction time of 6 ± 2 ns. This type of

463 excimer is formed from an ionized argon atom that combines with another stable argon
 464 atom. The second, which accounts for the other 75% of light yield, is done through a Σ
 465 triplet excimer excitation and has a reaction time of $1590 \pm 100 \mu\text{s}$. The triplet state excimer
 466 is formed from a stable argon atom, an ionized argon atom, and a free electron.^[1] Since the
 467 prompt scintillation light is orders of magnitude faster than drift time from the TPC signal
 468 this information can be used to address this ambiguity.

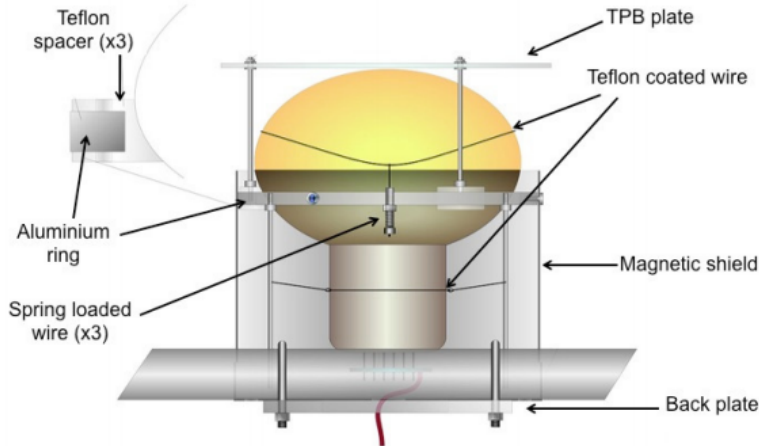


Figure 3.9: Schematic of a PMT optical unit for MicroBooNE.

469 The MicroBooNE light collection system consists of 32 8-inch diameter Hamamatsu
 470 R5912-02mod cryogenic PMTs. The PMT's are not optimized to detect 128nm vuv light.
 471 Therefore, an acrylic plate coated with tetraphenyl butadiene(TPB)^[2] was installed in front
 472 of the PMT's to act as a wavelength shifter. The TPB plate absorbs the 128nm light and
 473 re-emits it a peak wavelength of 425nm. Also, it is known that PMT response is reduced
 474 from certain orientations in the earth magnetic field. To address this a mu-metal shield was
 475 designed to extend just past the equator of the PMTs. A schematic of a PMT optical unit
 476 is shown in figure 3.9.

477 The PMT system is mounted on a railing behind the wire planes and spans the entire
 478 detector length as shown in figure 3.10. This also provides a weak handle on interaction
 479 position since the scintillation light is fairly localized. Most importantly, since MicroBooNE
 480 is a surface detector and constantly being bombarded by cosmic rays, the scintillation flash

481 is used as a method of identifying neutrino interactions coming in time with the beam.



Figure 3.10: PMT optical units installed on support racks inside the MicroBooNE cryostat

482 3.5 Electronics Readout

483 The TPC and PMT systems produce detector analog signals which need to be digitized,
484 transferred out of the detector, and written to disk through data acquisition(DAQ) software.
485 Both systems perform a first round of shaping and amplification in the cold LAr and then
486 interface with warm electronics for further processing. The DAQ continuously writes to disk
487 and creates a buffer which stores data for up to 24 hours. MicroBooNE employs various
488 triggers to signify beam and non-beam data blocks and permanently store data from the
489 buffer stream. A schematic overview of the TPC and PMT signal processing and readout
490 stages is shown in Figure 3.11.

491 For the TPC, a large portion of the electronics processing for the 8,256 wire signals
492 are performed directly in the LAr. To reduce electronics noise, the input distance from
493 the wires to the preamplifier is minimized. The sense wires directly interface with CMOS
494 analog front end ASICs which operate on cold motherboards. In total MicroBooNE has
495 516 CMOS ASICs. The ASICs generate 50 W of heat load which is a negligible impact on
496 the cryogenics system. The motherboards shape and amplify the low noise signal. There

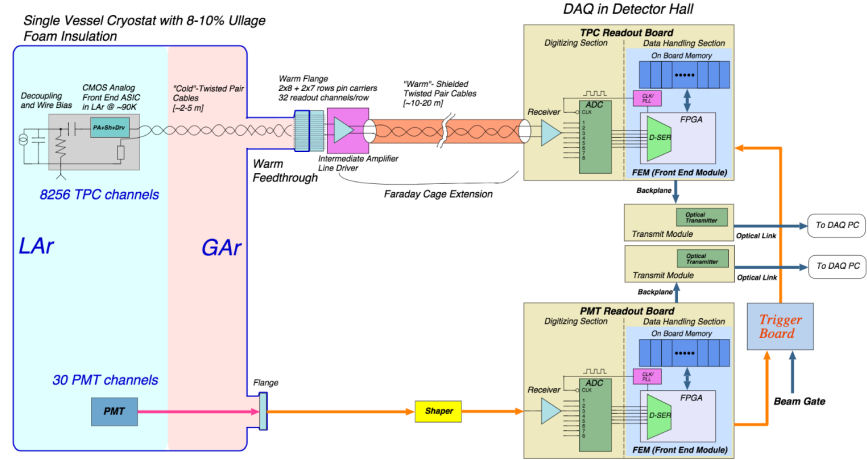


Figure 3.11: MicroBooNE LArTPC and PMT signal processing and readout schematic.

497 are 36 top style motherboards that instrument Y,U and V plane wires and 14 side style
 498 motherboards that instrument U and V plane wires. The signals are then passed through a
 499 series of 12 feedthrough ports to warm electronics. The warm signals are then distributed
 500 over nine readout crates, which digitize the signals.

501 The TPC system read out frame is defined to be 1.6 ms. This number was chosen
 502 to account for ionization electrons that are generated at the cathode and drift the entire
 503 distance to the wires in the presence of a 500V/cm E-Field. In MicroBooNE, an event is
 504 defined as four 1.6 ms readout frames. The additional frames allow for identification of
 505 cosmic particles that arrive before and after the neutrino interaction.

506 The PMT system is also processed in a similar fashion. The PMT's undergo 60 ns
 507 shaping to allow for precise measurements of the signal rising edge. The signals are sampled
 508 at 64MHz but only shaped signals above a threshold are read out and stored for data. The
 509 PMT signals are split into two different gains. A high gain signal that is 10 times the
 510 amplitude of the low gain. The signals are then brought to pre-amp/shaper boards and
 511 digitized and sent to the DAQ.

⁵¹² **Chapter 4**

⁵¹³ **Booster Neutrino Beam**

⁵¹⁴ Fermilab is one of the world's leading neutrino facilities and currently produces two neutrino
⁵¹⁵ beams that span a wide range of neutrino energies. The Booster Neutrino Beam (BNB),
⁵¹⁶ which will be described in detail throughout this chapter, is a lower energy beam that
⁵¹⁷ delivers neutrinos to various short baseline experiments. Fermilab also hosts the NuMI
⁵¹⁸ (Neutrinos at the Main Injector) Beam [] which produces neutrinos over a large range
⁵¹⁹ between 1GeV/c-30GeV/c and delivers neutrinos to various experiments both on-axis and
⁵²⁰ off-axis. The NuMI beam will not be covered in this thesis.

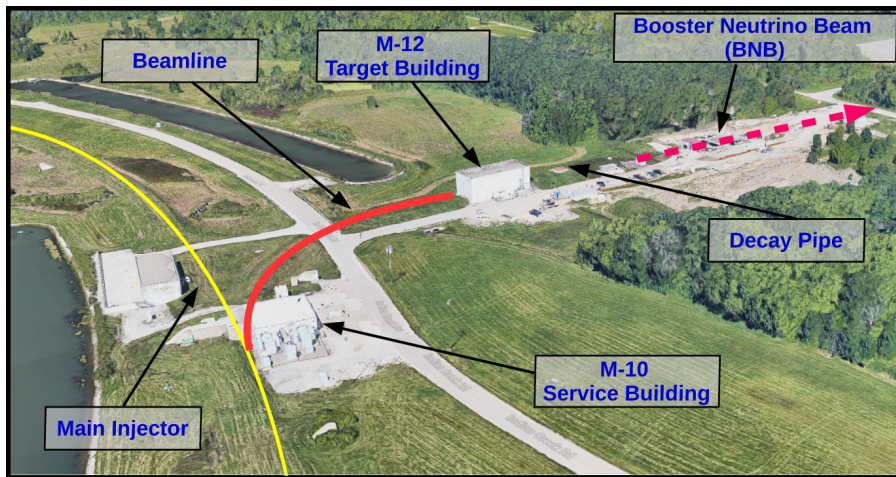


Figure 4.1: This image shows an aerial view of the Booster Neutrino Campus. Protons are extracted before the main injector near the M-10 service building and delivered to the M-12 target hall where the low energy neutrino beam is produced.

521 The Booster neutrino campus is illustrated in figure 4.1. To produce the BNB, pro-
522 tons are extracted from a transfer line just prior to the main injector and then interact
523 with a beryllium target. The following sections will describe the beam system, neutrinoos
524 production process, and flux predictions for the BNB.

525 4.1 Primary Beam, Target and Horn

526 The BNB extracts 8.89 GeV/c momentum protons from the Fermilab Booster synchrotron
527 and delivers them to a beryllium target housed in the M-12 building. The protons from
528 the booster are grouped in 1.6 μ s windows called 'beam spills'. One beam spill contains
529 approximately 5×10^{12} protons. On average the Booster can run no more 5 Hz with no
530 more than 11 pulses in a row at 15 Hz. In optimal running conditions the Booster can
531 deliver 9×10^{16} protons on target (P.O.T) per hour.

532 The beam pipe directly leading to the target is approximately 5 feet long and is held
533 under vacuum to minimize proton interactions not originating from the target. The incom-
534 ing proton flux is measured by a pair of toroids which are positioned upstream of the target
535 and provide an error on P.O.T on the order of 2 %.

536 The target consists of 7 cylindrical beryllium slugs that together produce an effective
537 cylinder of 71.1 cm in length and 0.51 cm in radius. The use of multiple slugs gave the
538 beryllium more surface area to allow efficient heat transfer from a simple air cooling system
539 to be sufficient. An exploded view of the BNB target is shown in figure 4.2. As the protons
540 collide with the beryllium, large amounts of secondary and tertiary mesons, such as π^\pm, K^\pm ,
541 are produced . These mesons will later decay into neutrinos and other decay particles.

542 The target is positioned inside of a large toroidal electromagnet called a horn. The horn
543 is made of an aluminum alloy (6061 T6) and is pulsed with 174 kA of current to produces
544 a $1/R$ field where R is the distance from the axis of the horn. Since neutrinos are neutral
545 particles and can not directly be focused by an electric or magnetic force. Instead, the horn
546 focuses the proper sign parent π^\pm, K^\pm in such a configuration that the neutrino angle from
547 the parent decay particles are focused in a beam.

548 Directly downstream of the horn/target assembly is a collimator that is used to reduced

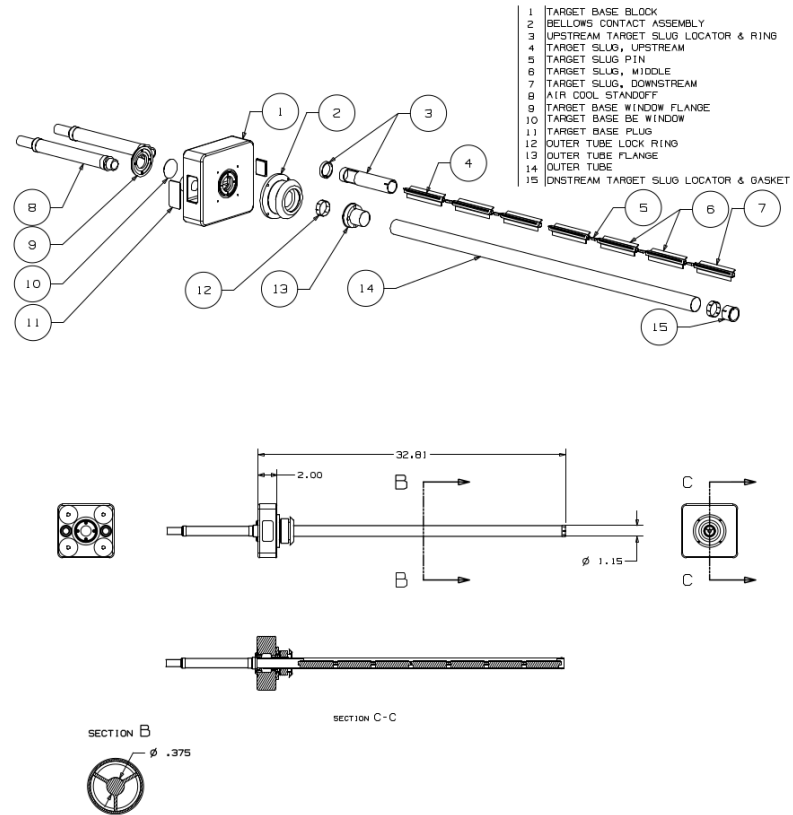


Figure 4.2: An exploded view of the BNB target which shows the 7 Beryllium slugs housed inside the support structure.

background coming from unwanted particles. Particles passing through the collimator enter a 45 m long decay region. In this region, most of the particles decay to produce the neutrino beam. At the end of the decay region there is a beam stop made of steel, concrete. There is also an array of gas proportional counters to detect high energy muons that punch through the beam stop. A diagram of the entire BNB system is shown in figure 4.3. When the horn polarity focuses (negative) positive charged mesons a (anti)neutrino beam is produced.

4.2 Neutrino Flux Prediction

The neutrino flux prediction for MicroBooNE uses the same GENIE simulation files used by MiniBooNE. The files are feed into a Geant4 module that simulates the particles as they

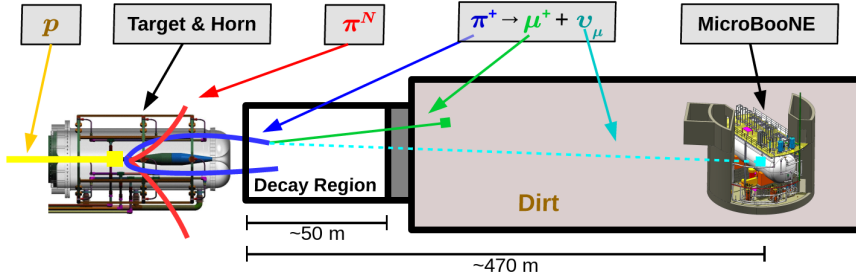


Figure 4.3: This figure shows the Booster Neutrino Beam line at FNAL. The neutrinos are produced in the decay region and then travel towards the MicroBooNE detector located 470 m down stream.

558 travel through the target, horn, and decay region. This produces a MC flux estimate for each
 559 of the various neutrino types. A systematics study was then performed to provide an error
 560 estimate for each of the ν_e , $\bar{\nu}_e$, ν_μ , and $\bar{\nu}_\mu$ flux predictions. To do this, 6 primary systematics
 561 were varied: the production rates of π^+ , π^- , K^+ , K^- , and K_L^0 , and a group systematic
 562 comprised of the horn current miscalibration, skin depth, nucleon inelastic, nucleon QE,
 563 nucleon total cross sections, pion inelastic, pion QE, and pion total cross sections. Beam
 564 errors for each of systematics are shown in Table 4.1 .The final flux estimate with the error
 565 uncertainty is shown in Figure 4.4.

	ν_μ	$\bar{\nu}_\mu$	ν_e	$\bar{\nu}_e$
Delivered P.O.T.	2.00%	2.00%	2.00%	2.00%
π^+	5.8%	0.46%	4.62%	2.66%
π^-	0.01%	7.51%	0.28%	3.20%
K^+	0.38%	0.13%	5.19%	2.61%
K^-	0.01%	0.35%	0.28%	3.92%
K_l^0	0.03%	0.27%	2.36%	22.59%
Other	5.78%	6.09%	3.6%	7.61%

Table 4.1: Systematic errors for production of various neutrino types with respect to their, P.O.T. , parent particle, and other variables.

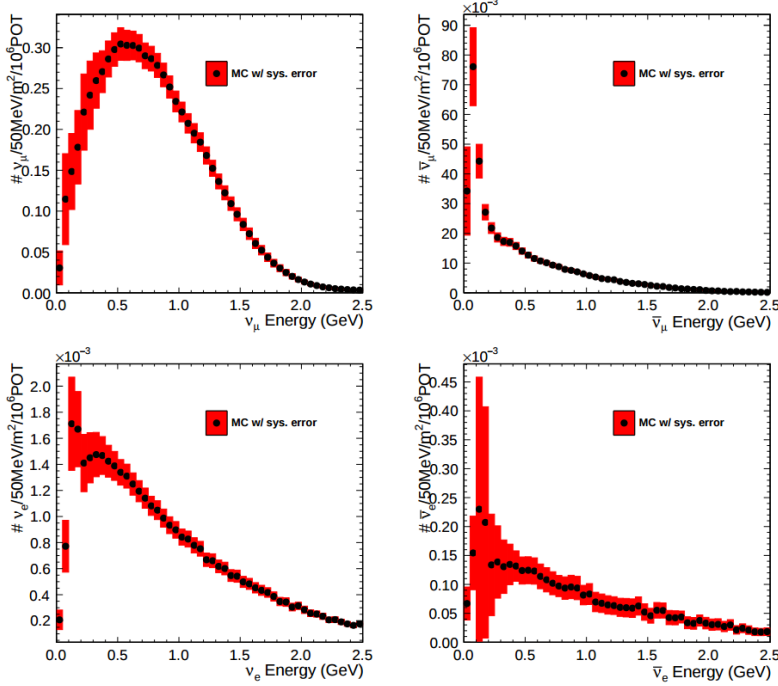


Figure 4.4: Monte Carlo flux predictions for the BNB neutrino spectrum. The red band represents the flux systematic errors. Note the orders of magnitude with the ν_μ spectrum rates.

⁵⁶⁶ Chapter 5

⁵⁶⁷ Low Energy Excess and Relevant ⁵⁶⁸ Cross Sections

⁵⁶⁹ 5.1 Overview

⁵⁷⁰ This chapter will discuss various facets of what is commonly called the “MiniBooNE Low
⁵⁷¹ Energy Excess.” First, we will present the anti-neutrino excess observed by LSND and how
⁵⁷² the oscillation results can be interpreted. Then, we will discuss the efforts of MiniBooNE to
⁵⁷³ understand the LSND results along with their oscillation results that establish the “Mini-
⁵⁷⁴ BooNE Low Energy Excess.” We will also discuss the neutral current $1\pi^0$ cross section
⁵⁷⁵ which is the dominant background in the oscillation analysis claims for both MiniBooNE
⁵⁷⁶ and LSND. Finally, we will discuss MicroBooNE’s role towards addressing understanding
⁵⁷⁷ the low energy excess claims of MiniBooNE.

⁵⁷⁸ 5.2 LSND Excess

⁵⁷⁹ The Liquid Scintillator Neutrino Detector (LSND) was a 167 ton neutrino detector stationed
⁵⁸⁰ at Los Alamos National Lab (LANL) designed to study neutrino oscillations. The detector,
⁵⁸¹ which hosted 1220 PMT’s for event detection, was place 30 m away from the source of a
⁵⁸² low energy (40 MeV) $\bar{\nu}_\mu$ beam. Using the Los Alamos LAMPF beam, 800 MeV protons
⁵⁸³ interacted with a water target to produce π^+ mesons which decayed into $\mu^+ + \nu_\mu$. The μ^+

would then interact with a copper beam stop and decay at rest to produce the low energy $\bar{\nu}_\mu$ beam.

The detector medium was primarily carbon (mineral oil CH_2). LSND could easily distinguish between electromagnetic showers (electrons/positrons/photon) or tracks (pi- μ s/muons/protons) by differences in the Cherenkov cone that was produced. The oscillation signal interaction was $p + \bar{\nu}_e \rightarrow n + e^+$. The primary e^+ is easily visible from the Cherenkov light it produced but a neutron will not produce Cherenkov light and therefore be invisible to the detector. The organic scintillator b-PDB was dissolved to the mineral oil at a concentration of 31 mg/l. The scintillator allowed the 2.2 MeV photon from the capture of the neutron on hydrogen to be detected. This allowed LSND a unique signal to identify $\bar{\nu}_e$ interactions. It should be noted that the detector technology could not easily discriminate between photons, electrons or positrons induced electromagnetic showers.

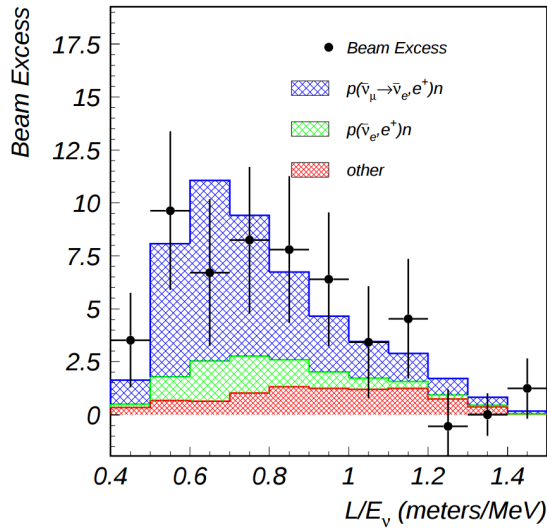


Figure 5.1: This is the LSND neutrino oscillation appearance plot as a function of L/E and represents the 87 event $\bar{\nu}_e$ excess claimed by the experiment.

596 In 2001, the collaboration published results for an observed excess of $87^{+22.4}_{-6.0}$ events
 597 above the predicted background as shown in figure 5.1. If the excess is interpreted as
 598 neutrino oscillations from a two neutrino model, the best fit of the excess would suggest a
 599 $\sin^2(2\theta) = 0.003$ and $\Delta m^2 = 1.2\text{eV}^2$ which greatly contradicts many other measurements
 600 for $\Delta m_{2,3}^2$ or $\Delta m_{1,3}^2$ [1]. One explanation for the excess suggests the idea of mixing between
 601 other additional neutrino states. These neutrinos are called ‘sterile’ since they cannot
 602 directly couple via weak interaction as mentioned prior from the constraints from LEP.

603 5.3 Miniboone Excess

604 The Mini Booster Neutrino Experiment(MiniBooNE) was designed to address the claims of
 605 the LSND $\bar{\nu}_e$ excess result. The MiniBooNE detector was a mineral oil Cerenkov detector
 606 designed to be a similar technology to LSND. MiniBooNE, stationed at FNAL in the BNB,
 607 was positioned 541 m from the neutrino source and was able to receive both ν_μ and $\bar{\nu}_\mu$
 608 fluxes. The distance was chosen such that the L/E parameter were similar to that of the
 609 LSND experiment.

610 MiniBooNE, which contained 818 tons of mineral oil(CH_4), was located underneath
 611 more than 3m of earth overburden to help reduce cosmic rays. The detector supported a 35
 612 cm thick outer cosmic veto using 240 PMT’s. The veto efficiency was 99.99% for rejecting
 613 cosmic muons. The inside of the detector was instrumented with 1,280 8-inch PMT’s
 614 which were used to read out neutrino and comsic data. Cherenkov light from different
 615 particles produced distinct patterns on various PMT’s inside the spherical detector. A
 616 cartoon showing various type of signal topologies from the MiniBooNE detector are shown
 617 in figure 5.2. The detector energy scale was calibrated in situ by fitting various parameters
 618 from thoroughgoing muons, decay Michele electrons, and π^0 decays’s. A clear limitation of
 619 Cherenkov detectors is the inability to concretely distinguish between photon induced or
 620 electron induced showers.

621 The primary oscillation analysis for MiniBooNE was done ‘blind’ in an attempt to
 622 gain confidence from the physics community upon it’s findings. The entire analysis was
 623 developed on large statistics Monte Carlo simulation and a small sample of test data. In

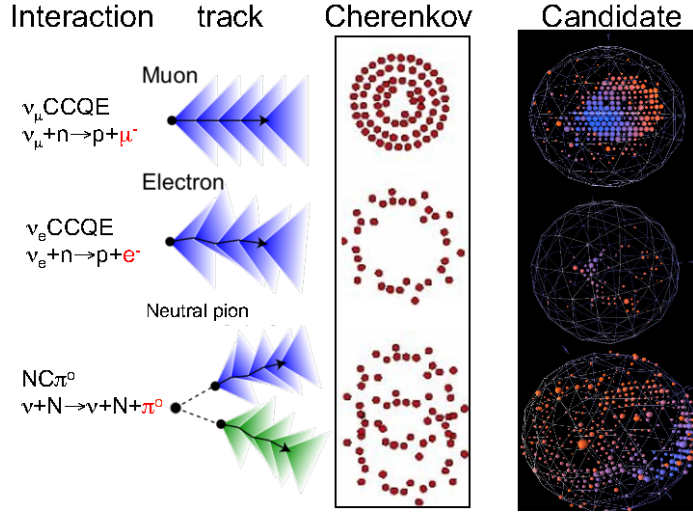


Figure 5.2: This cartoon depicts different particle interactions as observed in Cherenkov detector. The far right shows the interaction types as viewed in MiniBooNE

total, MiniBooNE accumulated 6.46×10^{20} P.O.T. of ν -data and 11.27×10^{20} P.O.T. of $\bar{\nu}$ -data. Fermilab's ability to support both neutrino and anti-neutrino beams allow for MiniBooNE to confirm that an LSND-like excess was independent of neutrino type. The data is in good agreement between signal and background predictions and contradicts the LSND claim up to 98% confidence in both modes above 500 MeV. The excess is most prominent in the region of events below 500 MeV, as seen in figure 5.3. In this region the largest background comes from π^0 -misidentification followed by photons coming from radiative Delta decays. MiniBooNE reports a total excess of 240.0 ± 62.9 combine $(162.0 \pm 47.8\nu, 78.4 \pm 28.5\bar{\nu})$ events in the neutrino energy range $200 < E_\nu^{QE} < 1250$ MeV. Also, if the excess is interpreted as a two flavor oscillation the inferred parameters are consistent with the LSND result.

5.4 Neutral Current π^0 production

The leading background from the MiniBooNE oscillation result, as mentioned in chapter 5.3, is π^0 -misidentification. Accurately measuring the neutrino induced neutral current single π^0 production cross section is therefore crucial in understanding background contributions for an oscillation analysis. Charge current π^0 production conveniently has an outgoing

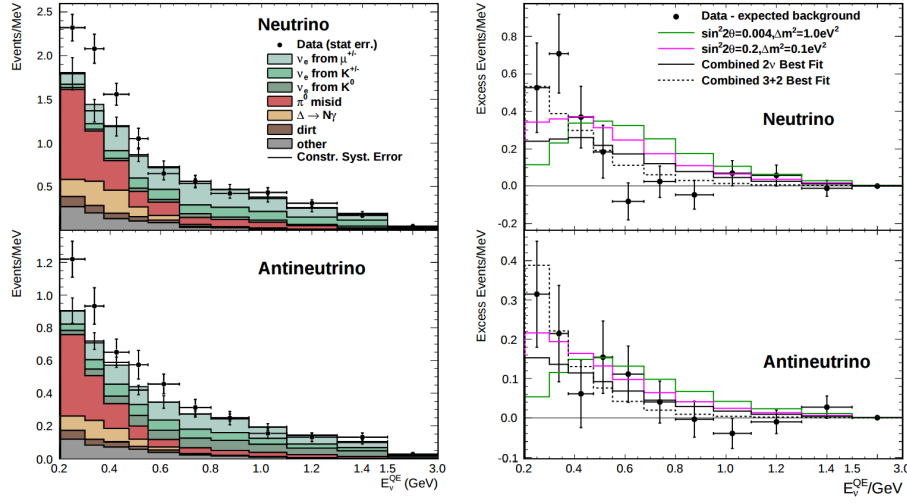


Figure 5.3: The left plots show the stacked histograms for signal and background overlaid with data for both neutrino and anti-neutrino modes. The right plots show the relative excess as a function of neutrino energy and make obvious the energy range that drives the excess.

639 charged muon in the final state and is very easy to identify. On the other hand, neutral
 640 current π^0 production does not guarantee any outgoing charged particles and therefore,
 641 makes identification much harder. For neutrinos in the BNB, the main production mode
 642 for neutrino induced neutral current π^0 production is via the $\Delta(1232)$ resonant production.
 643 Resonant production is when a baryon, such as a proton or neutron, are excited to a higher
 644 resonance state and then subsequently decays back to the initial state while liberating a
 645 π^0 . There are other neutrino induced π^0 production modes that MicroBooNE is sensitive to
 646 such as deep inelastic scattering and coherent production, but have a lower production cross
 647 section at the given BNB neutrino energy range. A general Feynman diagram can be used to
 648 describe the main components of neutrino induced neutral current single π^0 production in
 649 argon as seen in Figure 5.4.

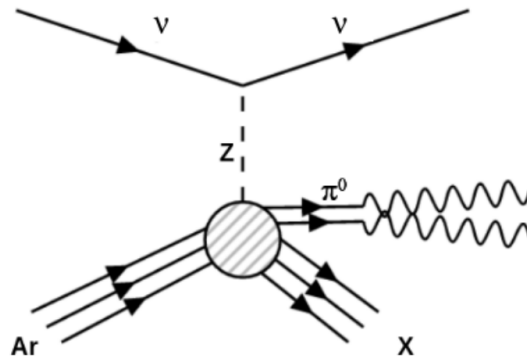


Figure 5.4: Neutrino induced single π^0 production on argon. This topology is defined such that 1 π^0 is produced and the other particles leaving the interaction (X) must only consist of nucleons.

650 5.5 NC-Pi0 in Carbon vs Argon

651 In 2010, MiniBooNE measured the total neutral current single π^0 cross section on carbon
 652 with what is currently the worlds largest statistics sample of π^0 s. The MiniBooNE neutral
 653 current single π^0 signal is defined as a topology that produces one and only 1 π^0 in the
 654 final state with no other other charged leptons or mesons originating from the vertex. In
 655 2015, the first measurement of neutrino induced neutral current π^0 production on argon was
 656 measured by ArgoNeut collaboration at Fermilab while running in the NuMI neutrino beam.
 657 AgroNeut, being a smaller detector, could not easily contain many of the electromagnetic
 658 showers from π^0 decays. This forced the analysis choose a slightly different final state signal
 659 definition requiring there to be at least one π^0 , no electron or muon, and allowing there
 660 to be any number of mesons in the final state. This modified signal definition makes any
 661 comparison to other historical data very complicated.

662 MicroBooNE, which resides in the same neutrino beam line as MiniBooNE, is a prime
 663 candidate for various studies of neutral current π^0 production studies between different
 664 target materials(C/Ar). Being a larger LArTPC, more π^0 decays will be contained allowing
 665 for high statistics measurements of the cross section along with the general need to measure
 666 the production rate as input to its own oscillation analysis.

667 Chapter 6

668 Cosmogenic π^0 's at MicroBooNE

669 In this chapter we will talk about some of the challenges and interesting physics cases re-
670 garding cosmogenics in a surface LArTPC. Many cosmic ray particles penetrate surface
671 detectors and populate the detector region making it necessary to remove these particles
672 from reconstruction and address charge contamination in neutrino events. The majority of
673 this chapter will emphasize cosmogenic induced electromagnetic showers and subsequently
674 π^0 selection. We will first examine some historical cosmogenic studies from the Icarus experi-
675 ment. Then, introduce what MicroBooNE can contribute in terms of understanding cosmics.
676 We will address the cosmic simulation that is used, various steps in reconstruction and pat-
677 tern recognition used to select π^0 's in a LArTPC. Finally, we will conclude with how these
678 studies impact future cross section analyses and backgrounds toward the low energy excess
679 analysis.

680 6.1 Motivation

681 Cosmogenic particles allow for a separate test of reconstruction tools along with an inde-
682 pendent way to address detector energy scale. The high rate of surface cosmics do indeed
683 cause some trouble with disentangling signal neutrino events so cosmic ray removal Luckily,
684 surface cosmogenic samples allow for a large statistics dataset to develop and optimize re-
685 construction techniques. Cosmogenic muons that traverse the detector provide a handle to
686 understand detector energy scale along with understanding track reconstruction efficiency.

687 Stopping muons that produce a Michele electron help provide a benchmark for low energy
 688 showers in the 10's of MeV range. The π^0 resonance, with a mass of $134.9\text{MeV}/c^2$, can be
 689 used as a standard candle to benchmark overall detector energy scale.

$$\mathcal{M} = \sqrt{2E_1E_2(1 - \cos\theta_{12})} \quad (6.1)$$

690 Electromagnetic shower reconstruction for LArTPC's is well known to be a hard task.
 691 The high resolution of the 2-dimensional projections of EM-showers introduce many chal-
 692 lenges to develop unbiased and fully automated reconstruction. In 2001, the T600 ICARUS
 693 detector ?? performed a surface test run in Pavia, Italy. During this 100 day test the detec-
 694 tor collected over 30,000 cosmic ray events. In 2008, the ICARUS collaboration published
 695 a study of electromagnetic showers coming from π^0 decays in the Pavia dataset. To select
 696 candidate π^0 events, ICARUS hand scanned a total of 7,500 potential events from a PMT
 697 triggered sample. Their hand scanning requirements included, that at least two well sep-
 698 arated electromagnetic showers were visible, a valid t_0 time for the vertex, and that there
 699 was not much charge contamination coming from a nearby cosmic muon. After this, they
 700 were left with 212 ‘hadronic interactions with at least one candidate neutral meson’ which
 701 they then proceeded to reconstruct. Their final reconstruction consisted of energy scaling
 702 to account for missing charge in the shower and a minimization against the true π^0 mass
 703 (134.9). An example of one of their hand scanned clustering events is shown if Figure 6.1.

704 MicroBooNE, being a surface detector, is in a position to do a similar study with im-
 705 proved reconstruction techniques. Also, understanding the cosmic production rate for single
 706 π^0 's is valuable to any MicroBooNE analysis that involves EM-showers. The following sec-
 707 tions will present MicroBooNE's Monte Carlo simulation and state of the art reconstruction
 708 techniques.

709 6.2 Monte Carlo Simulation

710 The MicroBooNE cosmics Monte Carlo is generated by CORSIKA(COsmic Ray Simula-
 711 tion for KAscade) v-7.4003[?] CORSIKA simulates particles coming from a wide range of

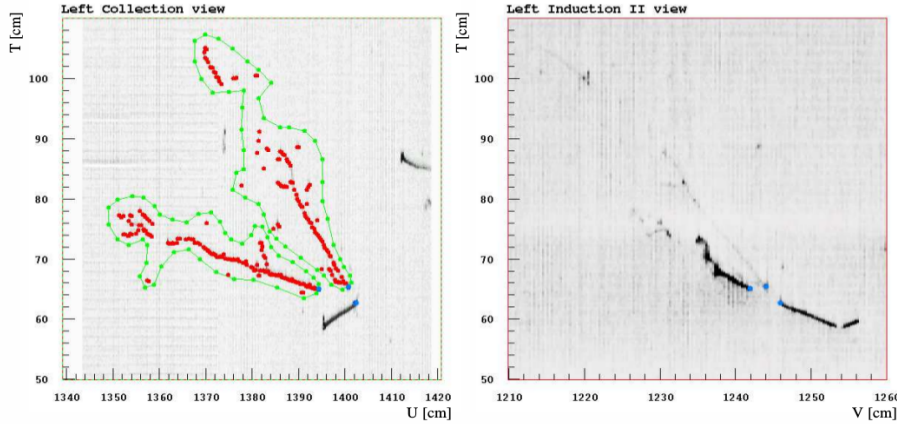


Figure 6.1: A cosmic π^0 from the ICARUS Pavia run. The left image, shows the hand drawn clustering and positions of the shower conversion point and vertex point. The right image, shows the same event on a different wire plane view.

interactions initiated by cosmic ray particles in the upper atmosphere. The simulation is robust and accounts for various input parameters such as, longitude and latitude, elevation, and the earth's magnetic field. The particles are simulated over a large region above the detector complex but only particles that travel through the detector cryostat volume are kept. The passage of these particles simulated by the GEANT4 package. Cosmic rays that do not travel through the cryostat have a low likelihood of producing secondary or tertiary particles that enter the detector TPC volume[?]

In one MicroBooNE drift window(2.3ms) there are on average 6 cosmic muons. The muons do not directly contribute to many EM-showers but sometimes pass through an EM-shower from another particle. For MicroBooNE, the vast majority of muons are through-going and do not lead directly toward any method of π^0 production.

Various other particles such as, protons, neutrons, and charged pions enter the TPC volume and may produce subsequent π^0 . A distribution of π^0 production process is shown in Figure 6.2. Nearly half of the π^0 's produced in the MicroBooNE TPC are produced through a neutron inelastic scattering.

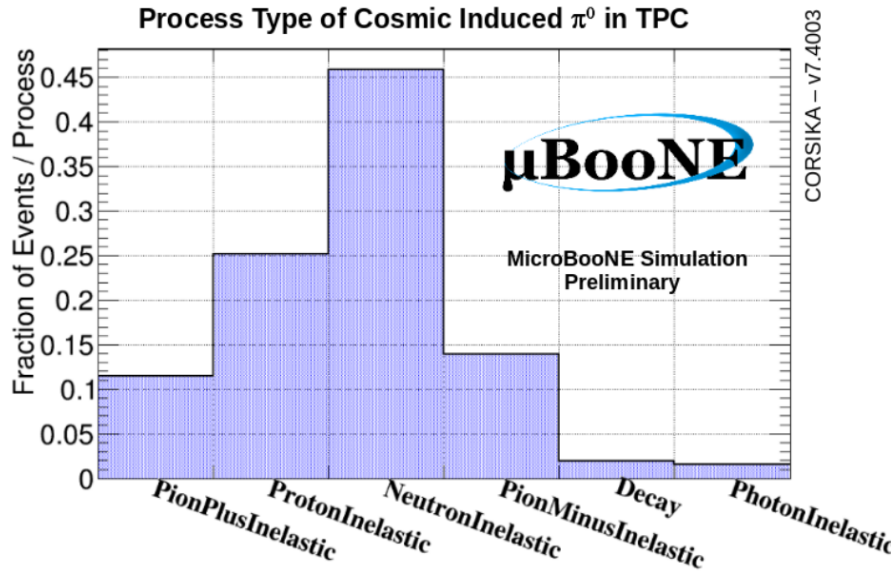


Figure 6.2: Physical process for cosmic π^0 that decay inside the TPC.

6.3 Traditional Reconstruction

The traditional approach for LArTPC reconstruction involves grouping drift charge that is deposited on the wires to form wire-hits. The light collection system also has light-hits which corresponded to collected light on an individual. A group of PMT's that have light-hits at the same time is called a flash. Hits from each of the wire planes are clustered together with various reconstruction algorithms to form reconstruction objects that relate to individual particles in the detector. There are two primary reconstruction objects: tracks, which are mostly linear and compact clusters that represent muons, protons, and charged pions, and showers which are more fuzzy shaped cluster objects that represent photons and electrons. Next, to reconstruction a 3D object, an algorithm must match the same 2D cluster objects in at least two of the three wire planes. For MicroBooNE, and the general LArTPC community, matching track reconstruction well advance but shower reconstruction suffers many hurdles. In recent years lots of progress has been made for LArTPC shower reconstruction. Various different techniques such as: improved 2D clustering and matching techniques[], sophisticated pattern recognition tools[], and deep learning[] approaches have been explored with varrious strengths and weaknesses.

743 6.4 Wire Cell Imaging

744 The traditional approach is not the only way to reconstruct LArTPC data. Instead, wire
 745 data can be treated with a tomographic approach directly producing a set of 3D space
 746 points. Although computationally intensive, this approach allows for more information to
 747 be used in a 3D clustering framework which can directly impact shower reconstruction and
 748 mitigate degeneracies from the 2D matching method.

749 The Wire-Cell framework, spearheaded by Brookhaven National Labs(BNL), utilizes
 750 this approach to create 3D space points from MicroBooNE's TPC data. The approach
 751 relies on the assumption that the same amount of ionization charge is seen on each plane.
 752 In MicroBooNE this is done by reconstructing small time slices on each wire planes. Each
 753 time slice involves solving a charge equation for all possible hits with respect to the matrix of
 754 hits actually recorded in the time slice. The charge equation is shown in equation 6.2. The
 755 detector wire signals are represented in matrix W while all potential wire hits are contained
 756 in H. Nonzero values in the Q matrix will correspond to unique wire-plane intersections of
 757 charge, near zero values represent ghost hits due to degeneracies in the charge equation.

$$\begin{bmatrix} W_{u_1} \\ \vdots \\ W_{u_n} \\ W_{v_1} \\ \vdots \\ W_{v_n} \\ W_{y_1} \\ \vdots \\ W_{y_n} \end{bmatrix} = \begin{bmatrix} Q_{u_1}^{H_1} & Q_{u_1}^{H_2} & \dots & \dots & \dots & Q_{u_1}^{H_{m-1}} & Q_{u_1}^{H_m} \\ \vdots & \vdots & \ddots & \ddots & \ddots & \vdots & \vdots \\ Q_{u_n}^{H_1} & Q_{u_n}^{H_2} & \dots & \dots & \dots & Q_{u_n}^{H_{m-1}} & Q_{u_n}^{H_m} \\ Q_{v_1}^{H_1} & Q_{v_1}^{H_2} & \dots & \dots & \dots & Q_{v_1}^{H_{m-1}} & Q_{v_1}^{H_m} \\ \vdots & \vdots & \ddots & \ddots & \ddots & \vdots & \vdots \\ Q_{v_n}^{H_1} & Q_{v_n}^{H_2} & \dots & \dots & \dots & Q_{v_n}^{H_{m-1}} & Q_{v_n}^{H_m} \\ Q_{y_1}^{H_1} & Q_{y_1}^{H_2} & \dots & \dots & \dots & Q_{y_1}^{H_{m-1}} & Q_{y_1}^{H_m} \\ \vdots & \vdots & \ddots & \ddots & \ddots & \vdots & \vdots \\ Q_{y_n}^{H_1} & Q_{y_n}^{H_2} & \dots & \dots & \dots & Q_{y_n}^{H_{m-1}} & Q_{y_n}^{H_m} \end{bmatrix} \begin{bmatrix} H_1 \\ H_2 \\ \vdots \\ H_{m-1} \\ H_m \end{bmatrix} \quad (6.2)$$

758 Then, each ‘slice’ is stacked to it’s corresponding x position. This produces a set of 3D
 759 space points that can be used in pattern recognition algorithms to identify different particles
 760 in the data. All reconstruction is done with accounting for known detector dead regions,

761 the current state of MicroBooNE's signal and noise processing and imaging that requires a
762 minimum of 2 to be matched from the charge equation.

763 6.5 Pattern Reconcition

764 Various pattern recognition tools are needed to address MircoBooNE's TPC data but for
765 this analysis they can be generalized into two efforts, cosmic track removal and EM-shower
766 clustering. Both approaches require different techniques but we will focus on optimizing
767 shower reconstitution first. As an overview of this chapter, we will first explore reconstruc-
768 tion effects for a Monte Carlo sample of single particle photons in the detector. Next, a
769 similar approach will be done with single particle π^0 . Then, we will apply various track re-
770 moval algorithms to understand their effects on shower reconstruction. Finally, we will run
771 a configuration of track and shower reconstruction over two samples of CORSIKA Monte
772 Carlo. A sample that contains neutron induced π^0 's in the fiducial region, and a back-
773 ground sample that contains various other background events. The fiducial bounds for this
774 analysis will constitute the volume between $-116. < y < 116.0$ and $400.0 < z < 1100.0$ and
775 spanning the entire drift (x) readout.

776 ADD IN SECTION OF METHOD FOR CLUSTERING

777 6.5.1 Shower Reconstruction

778 A sample of single particle photons were isotropically generated in the fiducial volume with
779 energies between an 0.01-2 GeV. The first step is to compare the effects that are derive
780 from the wire cell imaging stage. To do this we compare total deposited charge with total
781 reconstructed charge for the single particle sample to understand the resolution from wire
782 cell imaging. We find that there is a resolution of BLAH with bias BLAH.

783 6.5.2 Single π^0 Reconstruction

784 The vast majority(98.8%) of π^0 's decay into two photons. The relationship for the particle
785 mass, which was defined in eq6.1, shows the importance of properly account for the energy
786 and angle between the decay photons. To understand a baseline for reconstruction efficiency

787 we have generated a sample of 10000 single particle events isotropically throughout the
 788 detector volume with initial momentums spanning from 0 to 2 GeV.

789 First we will investigate energy deposited in detector from the decay. An plot of the true
 790 kinematic energy of photons from the decay particle is shown in Figure 6.3. It is important
 791 to note that both photons need to be reconstructed to form a mass resonance. This means
 792 that we are driven to optimize reconstruction to be robust around showers in the range
 793 of many 10's of MeV in deposited energy. Photons that convert near the fiducial edge of
 794 the detector can escape and deposit a small amount of energy in the detector. This poses
 795 problems for capturing the total amount of energy of the shower and drives the need for a
 796 fiducial cut around the edges.

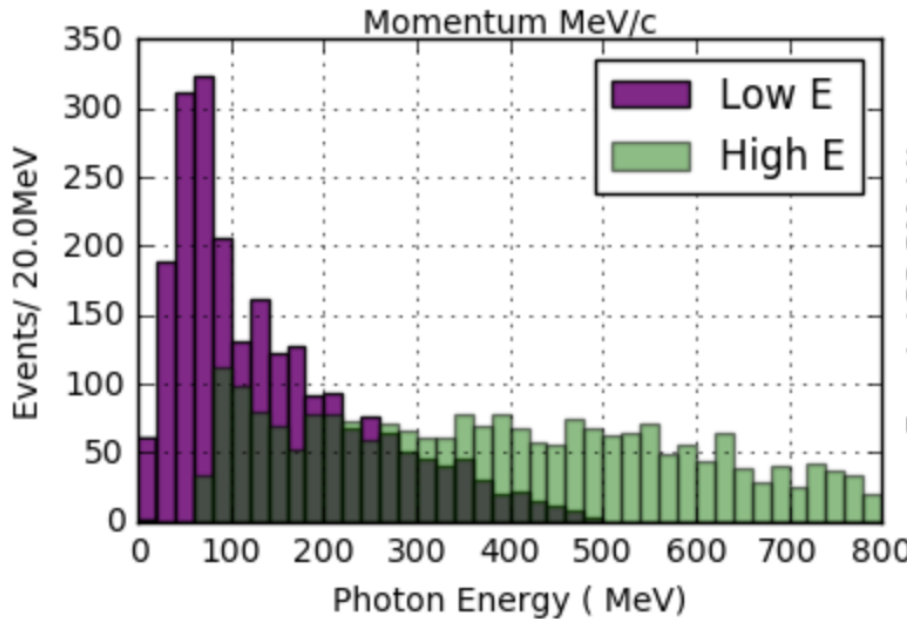


Figure 6.3: The

797 To plot reconstruction accuracy for the energy we are most interested in two metrics.
 798 The first, is the sum of energy collected between the two showers. This informs us that we
 799 are accounting for most of the energy deposited and handling the fiducial cuts well. The
 800 second, is the product of the two shower energies. This directly impacts the reconstructed
 801 mass resolution and informs us that we are properly clustering energy between the two

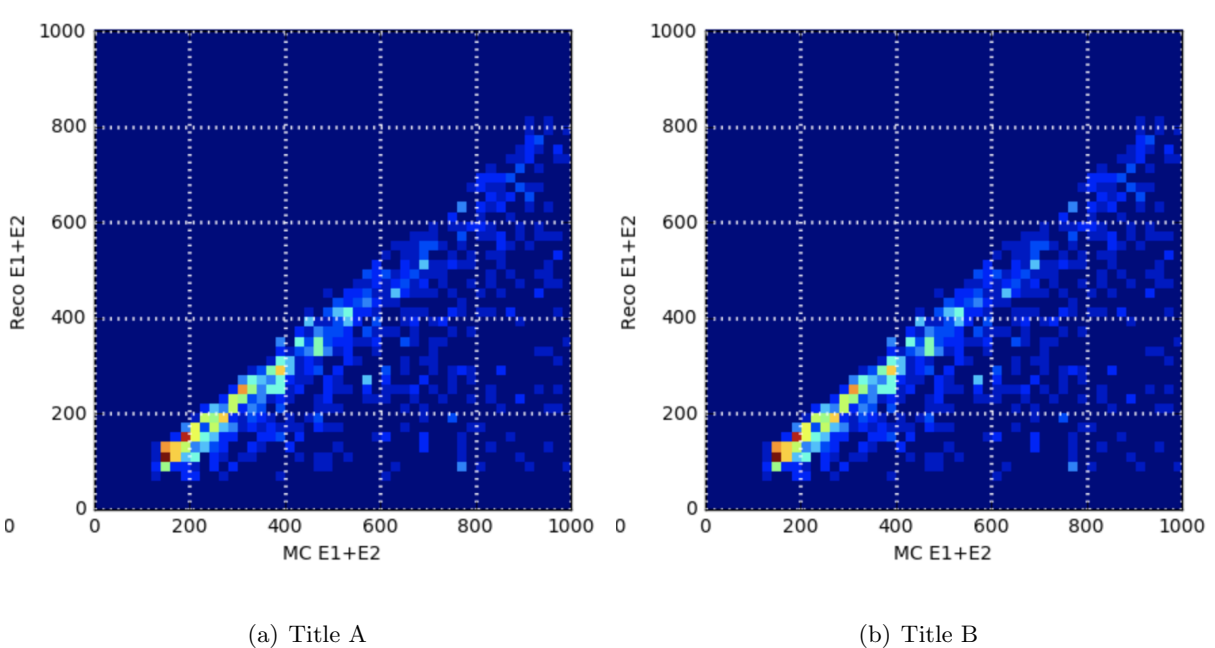


Figure 6.4: Reconstructed energy sum and energy product for shower pairs

showers properly. In figure 6.4 both metrics are plotted for reconstruction against true. Points along the diagonal represent accurate model predictions. As we will see later in this chapter, the energy product drives the width of the mass resolution.

805 Next we will investigate the effects of the opening angle between the two photons.
806 The minimum opening angle of the photons is constrained by the momentum boost as
807 the particle decays as shown in equation 6.3. The angular resolution is a very challenging
808 problem in LArTPC's using the traditional 2D projection approach. Fortunately, direct
809 3D reconstruction improves the angular resolution and allows for a better measurement of
810 shower direction.

$$\sin \frac{1}{2} \theta_{min} = \frac{M}{E_{\pi^0}} \quad (6.3)$$

811 A plot of the reconstructed vs true opening angle is shown in Figure 6.5. The $1 - \cos\theta$
 812 term from equation 6.1 is sensitive to tails of the mass distribution.

Finally we apply a final set of selection cuts. First, we require that the distance of closest approach between the two shower axis is less than 5 cm. This is to help ensure that

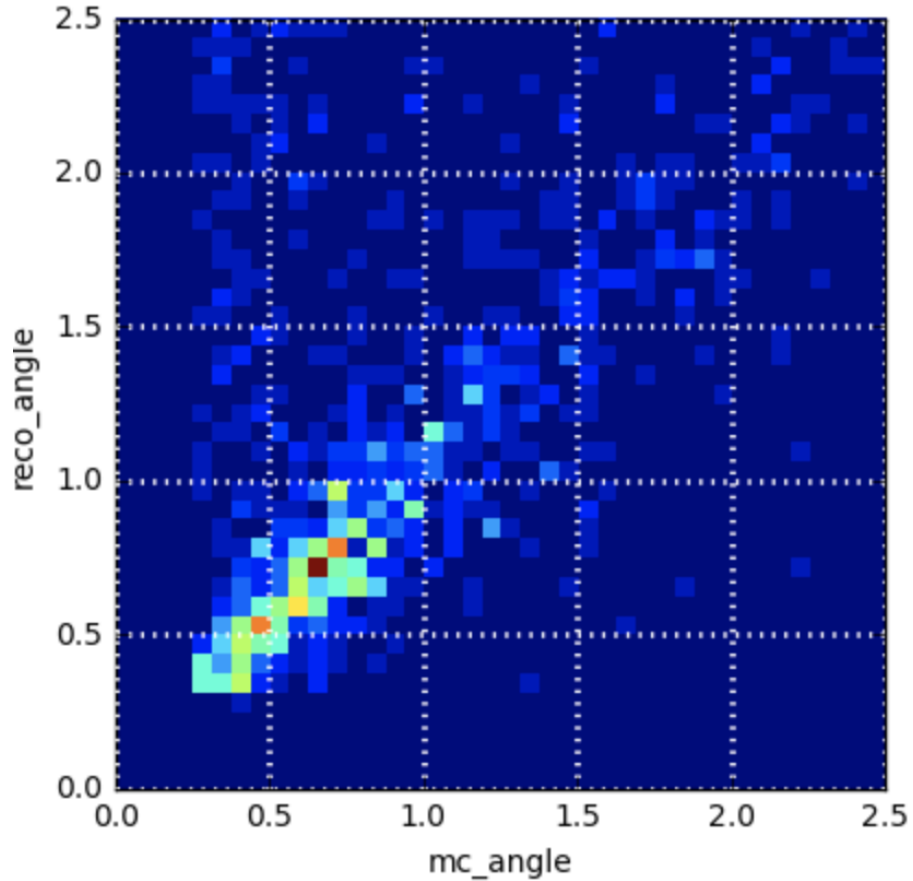


Figure 6.5: The

the photons are originating from a common origin. Next, the photon conversion distance can not be longer than 70cm. This is done to help identify showers that are correlated from the same decay. Finally we only accept showers that are above 50 MeV in reconstructed energy. Figure 6.6 shows the effect of various parameters as applied to the reconstruction. We find that the deficit in mass peak is mainly due to the energy reconstruction. This is due to clustering effect from missing energy.

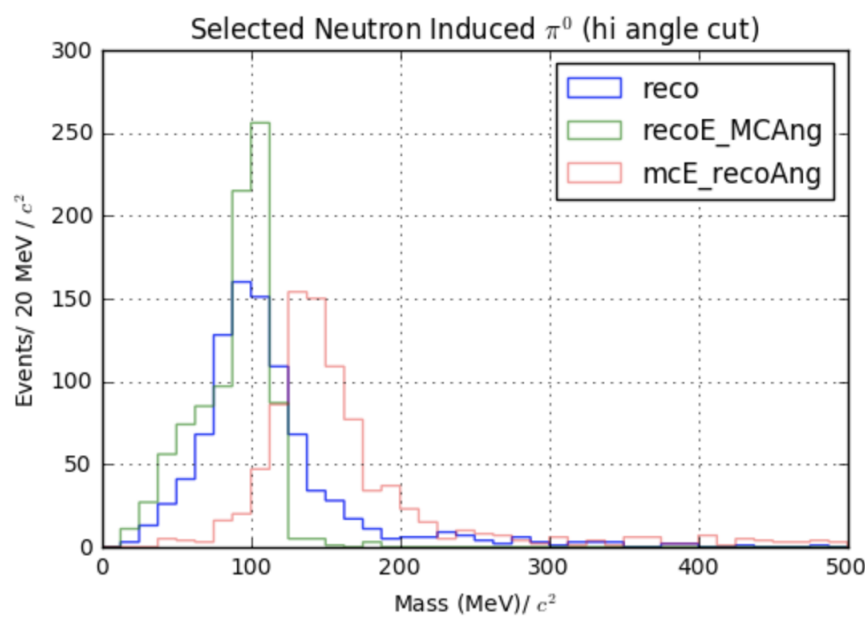


Figure 6.6: The

821 Chapter 7

822 Results

823 7.1 Reconstructed Variables

824 What are we going to plot:

825 Mass Peak

826 Opening angle

827 Energy Resolutions

828

829 7.2 Performance

830 Comment on efficenct possibly an MC scale argument for NCpi0 estimate.

831 **Chapter 8**

832 **Conclusions**

833 **8.1 Conclusion**

834 We see that using a 3D approach is powerful in terms of reconstruction. more importantly
835 we see the capilites of shower reconstruction with an LARTPC, and we see the extension
836 of how this work leads to an NCpi0 cross section someday.

837 **8.2 Outlook**

Part I

838

Appendices

839